

**Noninvasive hepatic lipid quantification with magnetic resonance imaging and spectroscopy**

by

Muhammad Salar Arif Khan

A thesis submitted to the Graduate Faculty of  
Auburn University  
in partial fulfillment of the  
requirements for the Degree of  
Master of Science

Auburn, Alabama  
May 04, 2019

Keywords: Hepatic, Resonance, Spectroscopy,

Copyright 2019 by Muhammad Salar Arif Khan

Approved by

Adil Bashir, Chair, Associate Professor of Electrical and Computer Engineering  
Thomas Denney, Professor of Electrical and Computer Engineering  
Stanley Reeves, Professor of Electrical and Computer Engineering

## Abstract

Excessive accumulation of intra-hepatocellular lipid (IHCL) can lead to one of the most common forms of chronic liver diseases in adults, the non-alcoholic fatty liver disease (NAFLD), that comprises a range of liver disorders including hepatic steatosis, an advanced stage of which can result in liver cirrhosis. Many diseases are known to be associated with the retention of IHCL including, but not limited to, obesity and type II diabetes. It is, thus, essential to quantify IHCL for early diagnosis and monitoring for an effective treatment. This study presents a non-invasive, robust and reproducible approach to quantify IHCL content using the single-voxel  $^1\text{H}$  magnetic resonance spectroscopy (MRS) and magnetic resonance imaging (MRI) at 3 Tesla (3T).

The study is divided in two parts: the MRS and the MRI investigations. Both parts used the constructed peanut oil phantoms of known fat fractions (8%, 14%, 18%, 25%, 30%, 40%, 45%, 55%) to test for validation and accuracy. The results with the peanut oil phantoms were in close agreement with the known fat fraction values ( $<10\%$  error on the fat fraction value).

The in-vivo MRS study included fifteen volunteers whose IHCL data was obtained at three different voxel locations in the liver with T2 corrections using five echo times (24, 30, 35, 40, 50 ms). The study confirmed the obese volunteers with fatty liver, registering IHCL content beyond the 6% clinically considered normal range.

The in-vivo MRI study included liver data with similar protocol from multiple sites: Auburn University, University of Mississippi, Pennington University and University of Alabama at Birmingham. Existing schemes to model fat and water for separation into images were used to compute fat fraction images on which region of interest (ROI) was marked for analysis.

## Acknowledgments

I would like to thank my advisor, Prof. Adil Bashir, for providing me with the opportunity to learn from him throughout the course of this work. His dedication and commitment to the noble cause of research is a strong inspiration for me.

Many thanks to Prof. Reeves and Prof. Denney for being a part of my thesis research committee. Their contributions outside of this thesis work, in terms of discussions and course-works, have been instrumental for my professional growth.

Special thanks to Ronald Beyers for helping me understand the importance of safety and precaution with MRI equipment; and Julie Rodiek for always being there to assist me with anything at the MRI Research Center.

I am grateful to everyone involved at Pennington University, University of Mississippi and University of Alabama at Birmingham for their valuable contribution in the form of MRI datasets for this study.

Finally, I can not thank enough my sister, my parents and God Almighty for the unwavering love and support during this work and beyond.

## Table of Contents

Abstract . . . . .	ii
Acknowledgments . . . . .	iii
1 Introduction . . . . .	1
1.1 Problem statement and underlying motivation . . . . .	1
1.2 Aims and objectives . . . . .	2
2 Nuclear Magnetic Resonance . . . . .	3
2.1 Physics of NMR . . . . .	3
2.2 Relaxation times . . . . .	4
2.3 Spin Echo . . . . .	6
2.4 Gradient Echo . . . . .	7
2.5 Hardware . . . . .	8
3 Lipid quantification with MR Spectroscopy . . . . .	9
3.1 MR Spectroscopy principles . . . . .	9
3.2 Signal generation and pulse sequences . . . . .	11
3.2.1 Stimulated Echo Acquisition Mode . . . . .	11
3.2.2 Point Resolved Spectroscopy . . . . .	12
3.3 Study on Phantoms . . . . .	13
3.3.1 Peanut oil and liver lipid . . . . .	15
3.3.2 Phantom construction . . . . .	15

3.3.3	Experimentation and data acquisition on Phantoms . . . . .	16
3.3.4	Phantom data processing . . . . .	17
3.3.5	Phantom results and discussion . . . . .	18
3.4	in-vivo study . . . . .	20
3.4.1	Protocol enhancements . . . . .	20
3.4.2	T2 Correction . . . . .	23
4	Lipid quantification with MR Imaging . . . . .	29
4.1	Evolution of MR Imaging approaches . . . . .	29
4.2	Phantom Experimentation . . . . .	35
4.3	in-vivo study . . . . .	36
5	Conclusions and future recommendations . . . . .	43
	References . . . . .	45

## List of Figures

2.1	T2 Relaxation . . . . .	5
2.2	T1 Relaxation . . . . .	5
2.3	Spin Echo Pulse Diagram . . . . .	6
2.4	GRE Echo formation . . . . .	7
2.5	Auburn University MRI Research Center 7T facility . . . . .	8
3.1	Chemical environment of hydrogens in dichloroethane . . . . .	10
3.2	H-NMR spectra of di-chloro-ethane . . . . .	11
3.3	A typical STEAM sequence . . . . .	12
3.4	A simplified PRESS sequence . . . . .	13
3.5	Triglyceride formation . . . . .	13
3.6	Typical triglyceride molecule . . . . .	14
3.7	NMR Spectrum of a triglyceride molecule . . . . .	14
3.8	NMR spectra of a peanut oil phantom (left) and liver lipid (right) . . . . .	15
3.9	Phantoms in Water Bath (room temperature) for scan . . . . .	16
3.10	Voxel location on a vial in axial, coronal and sagittal planes . . . . .	17
3.11	Original and an Estimated MR Spectra . . . . .	18
3.12	Plots showing negligible scatter of measurements from known fat fractions in phantoms . . . . .	19
3.13	Scatter of phantom spectroscopic data scanned at UAB . . . . .	20
3.14	Three different voxels on the liver showing non-uniform lipid content . . . . .	21
3.15	T2 Correction on voxel 1 of volunteer 7 . . . . .	24
3.16	T2 Correction on voxel 2 of volunteer 7 . . . . .	24

3.17	T2 Correction on voxel 3 of volunteer 7 . . . . .	25
4.1	Leakage of fat signal in water image and vice versa . . . . .	30
4.2	Fat Fraction on Phantoms at 3T . . . . .	35
4.3	Pennington University - Liver Fat Fraction 3T . . . . .	37
4.4	University of Mississippi - Liver Fat Fraction 3T . . . . .	38
4.5	University of Alabama at Birmingham - Liver Fat Fraction 3T . . . . .	39
4.6	Auburn University - Liver Fat Fraction data-set #1 3T . . . . .	40
4.7	Auburn University - Liver Fat Fraction data-set #2 3T . . . . .	41
4.8	Auburn University - Liver Fat Fraction data-set #3 3T . . . . .	42

## List of Tables

2.1	Nuclei and their corresponding spins based on mass number . . . . .	3
3.1	Comparison of Phantom spectroscopy results from 3T and 7T . . . . .	18
3.2	UAB Phantom spectroscopy results from 3T . . . . .	19
3.3	5% CV improvement with shorter echo times . . . . .	22
3.4	4% CV improvement on the standard SIEMENS sequence with optimized breath-hold and PACE . . . . .	22
3.5	2% CV improvement with multiple TEs for T2 correction . . . . .	23
3.6	MRS Fat Fractions data summary . . . . .	27
3.7	T2 of Lipid and Water in-vivo . . . . .	28
4.1	Comparison of MR Spectroscopy with MR Imaging on Phantoms . . . . .	36
4.2	Protocol summary for multi-site liver fat fraction study . . . . .	36



## Chapter 1

### Introduction

#### 1.1 Problem statement and underlying motivation

Studies have confirmed that over the last decade, 20-35% of the US population has been known to be affected by the non-alcoholic fatty liver disease (NAFLD) and the numbers are further expected to rise [31] [32].

NAFLD is poised to become the leading chronic liver disease in the United States and the rest of the world with the disease ranging from steatosis to severe advanced forms such as the steatohepatitis and well beyond to fibrosis and cirrhosis [27].

Initially the deposition of fat in the liver was thought primarily to be due to alcohol abuse however, it has been understood and well-established that alcohol is not the only cause of fat retention in the liver and the risks that come with it. The association of the disease with insulin resistance, type II diabetes and particularly obesity is a major cause of concern as those in the advanced stages of NAFLD are believed to be strongly exposed to cardiovascular diseases including stroke and coronary heart disease [2][27]. A recent study has concluded about 70% prevalence of NAFLD in patients with type II diabetes [1] and another with 90% in diabetics and 70% in obese individuals [15].

As is the case with any disease, treatment demands an effective and efficient diagnosis. Currently, liver biopsy is the gold standard for liver fat quantification; however, major concerns with any biopsy procedure are the surgical risk, recovery time associated with it and sampling limitation to only a fraction of liver [39]. Moreover, patients with biopsy-proven NAFLD have shown a higher mortality rate than the general population [27].

Therefore, there is a dire need for a clinical non-invasive approach to not only diagnose but also monitor the disease as frequently as needed. This, precisely is the underlying motivation for the studies conducted in this thesis wherein non-invasive schemes are assessed for intra-hepatocellular fat quantification.

## 1.2 Aims and objectives

The primary goal of the study is to establish a reproducible and accurate way to quantify intra-hepatocellular lipid, non-invasively.

For that purpose, it is imperative to develop a standard spectroscopy sequence with improvisations for robustness and validation on phantoms and in-vivo studies. Spectroscopy is important as it illustrates information of metabolites and is necessary for an accurate quantification.

Secondly, an imaging modality needs to be explored that can image the abdomen. Existing schemes on model-based fat-water separation will be visited with liver data from multiple sites using similar imaging protocol for the in-vivo liver study.

## Chapter 2

### Nuclear Magnetic Resonance

#### 2.1 Physics of NMR

Subatomic particles such as the protons and neutrons have spins associated with them as they are known to be spinning on their own axis. In many nuclei, these spins are paired against each other such that the nucleus does not have a net or an overall spin. This is the case when an atom has an even number of protons and an even number of neutrons in its nucleus. However, if the sum of the number of protons and neutrons is odd, the nucleus is known to have a half-integer spin. A full-integer spin is associated with a nucleus that has both, an odd number of protons and an odd number of neutrons. Some examples are shown in table 2.1 below.

Nucleus	Protons	Neutrons	Mass number (Protons + Neutrons)	Spin	Natural Abundance
Hydrogen $^1\text{H}$	1	0	1	1/2	100%
Deuterium $^2\text{H}$	1	1	2	1	0.015%
Phosphorous $^{31}\text{P}$	15	16	31	1/2	100%
Oxygen $^{17}\text{O}$	8	9	17	5/2	0.04%

Table 2.1: Nuclei and their corresponding spins based on mass number

The spins are important since they indicate the possible orientations of the nucleus, for instance, half-integer spins could possibly have two orientations. When there is no externally applied magnetic field, the orientations are of equal energy but when an external magnetic field is present, the energies differ and typically, the bulk of the nuclei are in the lower energy level orientation [14].

By virtue of classical physics, a charged nucleus spinning around its own axis must have a magnetic moment at a microscopic level, however, random orientations of nuclei result in no significant magnetic moment macroscopically. Under external magnetic field, the bulk of the nuclei align with the direction of the external magnetic field, thus having a lower energy state. The nuclei whose magnetic moment opposes the external field are in the higher energy state but since they are always fewer in number, the net magnetic moment vector is aligned with the external field. Importantly, the axis of rotation of spinning nuclei precesses around the externally applied magnetic field. The frequency of this precession is called the Larmor frequency and is unique to each nucleus. It is given as:

$$\omega = \gamma B_0 \quad (2.1)$$

where  $\omega$  is the frequency of precession in Mhz,  $\gamma$  is the gyromagnetic ratio in Mhz/tesla and  $B_0$  is the strength of magnetic field in tesla.

If a system now is energized with a magnetic field in the transverse plane  $B_1$  at the Larmor frequency, nuclear magnetic resonance will occur. This  $B_1$  field is usually for only a few milliseconds and is called an radio-frequency (RF) pulse since it is in the radio-frequency range. It rotates the spin system which tips the net magnetization  $M_z$  from  $B_0$  direction to align it with  $B_1$ , developing a transverse component  $M_{xy}$ . The net magnetization  $M$  precesses around  $B_0$  back again after the  $B_1$  RF pulse is turned off. A receiver coil placed in the transverse plane can detect the changes in flux at the Larmor frequency and register a current signal, according to Faradays principle [14][16].

## 2.2 Relaxation times

The two kinds of relaxations that follow this principle are T2 relaxation and T1 relaxation. The time taken for the loss of magnetization in the transverse plane  $M_{xy}$  from 100% to approximately its 37% is the T2 relaxation. Figure 2.1 shows this relaxation time.

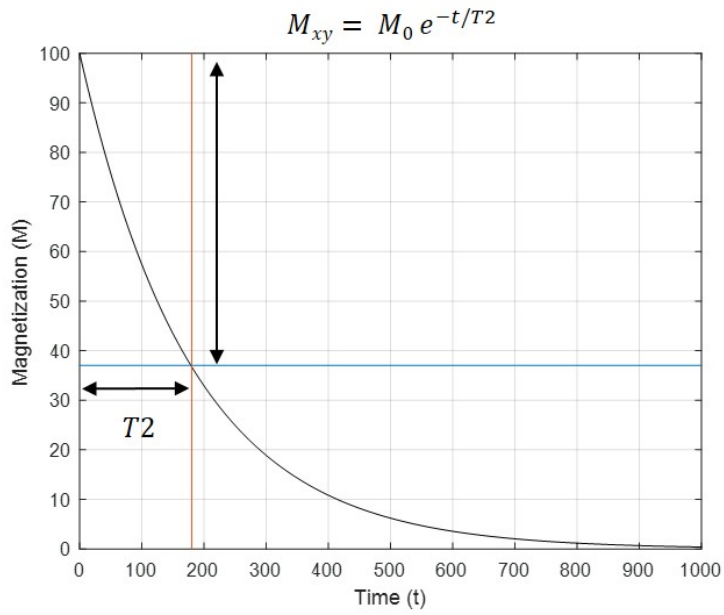


Figure 2.1: T2 Relaxation

After this T2 relaxation, the transverse magnetization is lost and the longitudinal magnetization is recovered. The time taken for the longitudinal magnetization  $M_z$  to reach approximately 63% of its maximum is the T1 relaxation time. This can be seen in figure 2.2.

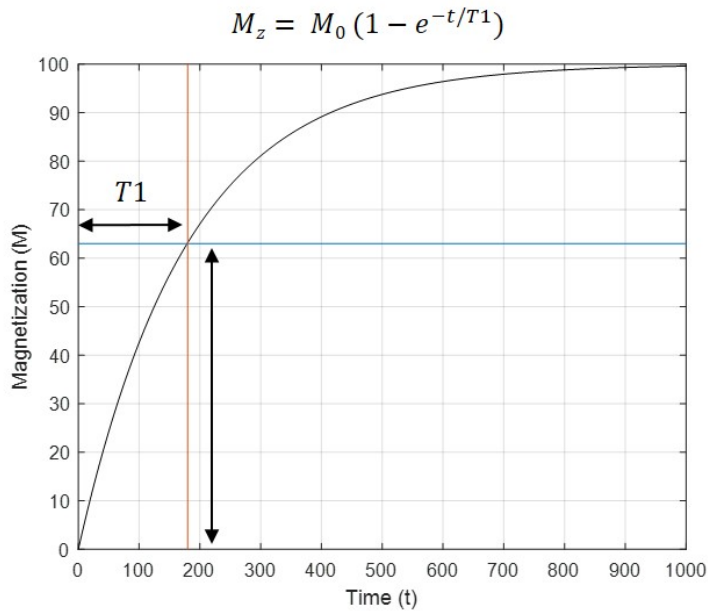


Figure 2.2: T1 Relaxation

Typically, the transverse magnetization decays faster than the predicted natural decaying phenomenon of the imaged tissue. This observed, effective or experimental value of T2 is

called the  $T2^*$  whereas the true hypothetical transverse relaxation is called the  $T2$ .  $T2^*$  encompasses the effects of molecular mechanisms and phase dispersion due to magnetic field inhomogeneities. The signal decay due to the  $T2$  relaxation is called the free induction decay or a FID. These FIDs can be used to create echoes.

### 2.3 Spin Echo

A 90 degrees RF pulse is going to generate a FID with an exponentially decaying transversal magnetization according to  $T2^*$ . However, a successive 180 RF pulse now will produce a Spin Echo SE. After the initial 90 degrees pulse, the transverse magnetization undergoes a decay largely due to the spins not precessing equally fast as some spins precess faster than others and gain some relative phase.

These faster spins leading in phase become slower and lag in phase after the second pulse of 180 degrees is applied. The 180 degrees pulse inverts the relative phases and allows the initially lagging spins to become the leading spins. Eventually, they rephase and result in a signal echo.

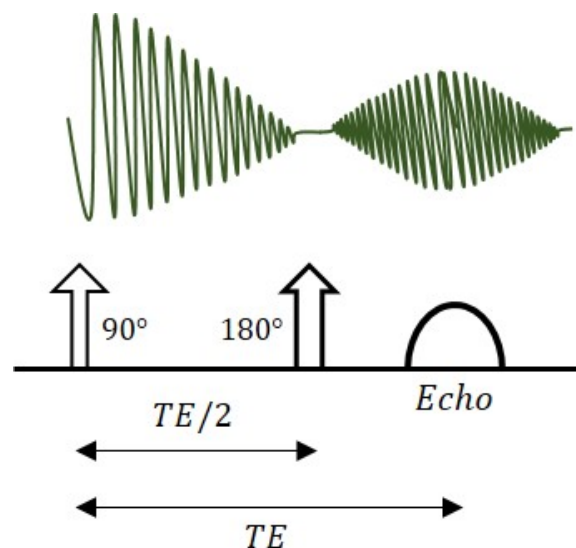


Figure 2.3: Spin Echo Pulse Diagram

Beyond this point, the faster spin echoes again lead the slower ones and the system de-phases again. The time taken between the first RF pulse and the signal echo is called the echo

time TE. Spin echoes may be formed with any flip angles with two successive RF pulses. Figure 2.3 below shows the application of these pulses and the corresponding echo formation.

#### 2.4 Gradient Echo

These are created with a manipulation of a FID using magnetic field gradients instead of RF pulses. After the excitation pulse, the FID decays with  $T_2^*$  but a dephasing gradient field is externally applied which causes an accelerated dephasing of the FID. The polarity of the gradient is then reversed with a rephasing gradient to undo the dephasing, thus, generating a signal. By adding further gradients, multiple gradient echoes may be formed. Figure 2.4 shows a timing diagram that illustrates one rephasing gradient after a dephasing gradient to generate a gradient echo.

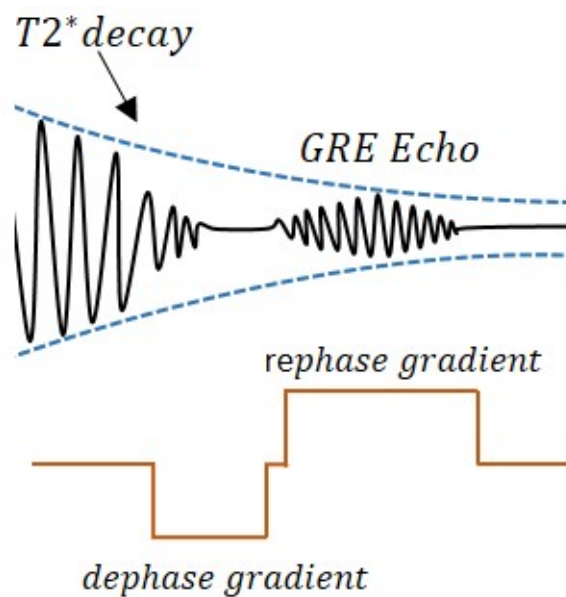


Figure 2.4: GRE Echo formation

## 2.5 Hardware

Experiments done in this thesis were performed using a Siemens clinical whole body Magnetom Verio 3T MRI system and a Siemens Magnetom 7T MRI system at the Auburn University MRI Research Center. Built in whole body coil was used for transmission of signal while body/torso coils were used for receive. The phantoms were scanned using a head coil. Figure 2.5 below shows a head coil in place at the 7T facility at the Auburn MRI Research Center.



Figure 2.5: Auburn University MRI Research Center 7T facility

Data from Pennington University was acquired using General Electric (GE) Medical Systems Discovery MR750w 3T scanner whereas the data from University of Mississippi was acquired with a Siemens Magnetom Skyra 3T scanner. The data acquisition from University of Alabama at Birmingham was with a Siemens Magnetom Prisma 3T scanner.



## Chapter 3

### Lipid quantification with MR Spectroscopy

This chapter focuses on spectroscopic perspective for lipid quantification with validation experiments on peanut oil phantoms and an in-vivo case study.

#### 3.1 MR Spectroscopy principles

Nuclear Magnetic Resonance Spectroscopy allows to determine the structure of a compound. This is possible due to a simple principle that proton signals are a function of their resonance frequencies. Each nucleus experiences a different chemical environment and thus resonates at a different frequency, thereby allowing to distinguish between different types of compounds. One of the phenomena that causes a difference in chemical environment is electron shielding; magnetic moments of electrons surrounding a nucleus can cause a distortion in the static magnetic field experienced by that nucleus, resulting in a slower precession which means a smaller resonant frequency. Thus, magnetic resonance spectroscopy exploits distinct positioning of nuclei within a molecule and its chemical environment to register signals as functions of their distinct resonant frequencies.

In figure 3.1, 1-1-dichloroethane can be seen to have two different types of hydrogens in terms of their chemical environments. The first set of hydrogens is shown in orange color which all have only one hydrogen (shown in blue) in their environment and that hydrogen nucleus may have its magnetic momentum aligned with the external magnetic field or it may be against it (only two possibilities exist), therefore, the registered signal for this first set of orange hydrogens is split into two lines of equal intensity: a doublet. The second set of hydrogen is shown in

blue color in figure 3.1 and this has three hydrogens (in orange color) in its chemical environment. Figure 3.1 shows that there are essentially four different types of magnetic combinations in which the three hydrogens can be magnetically aligned, thus, registering the signal as a quartet in the spectra shown in figure 3.2. Moreover, blue hydrogen's spectra appears further down the spectrum than the brown hydrogens because chlorine being more electro-negative, pulls the electron cloud towards it, deshielding and exposing the blue hydrogen to stronger magnetic field and thus, causing it to chemically shift more than the brown hydrogens on the spectrum.

The area under the spectra gives an estimate of the number of protons contributing to the signal. Thus, for quantification of any metabolite, the spectra are always integrated to find an estimate of the proton density.

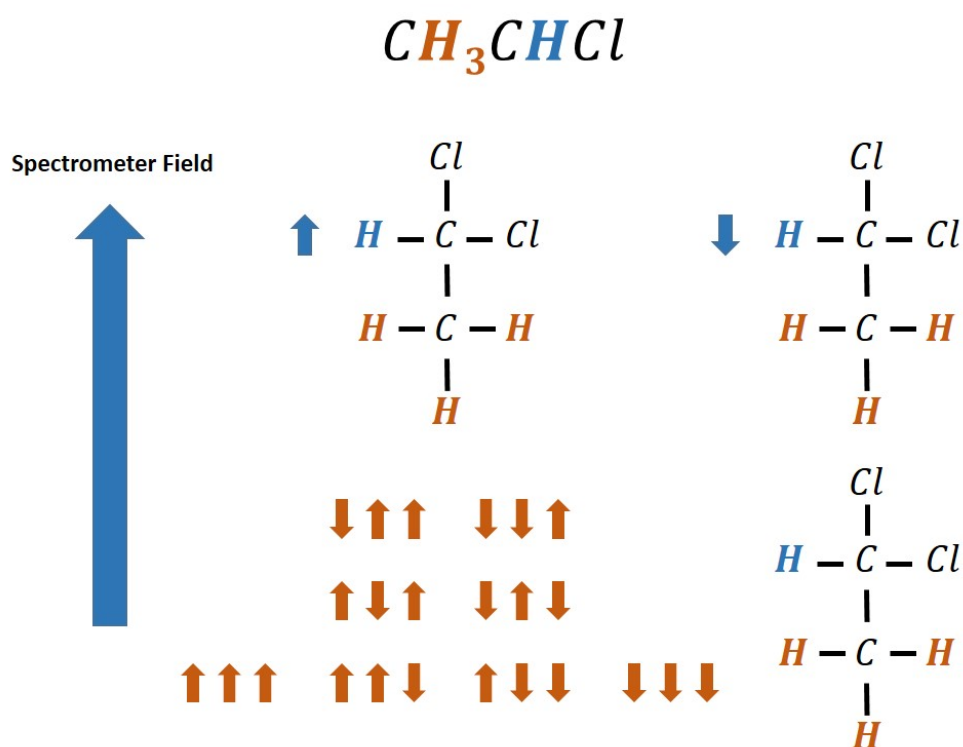


Figure 3.1: Chemical environment of hydrogens in dichloroethane

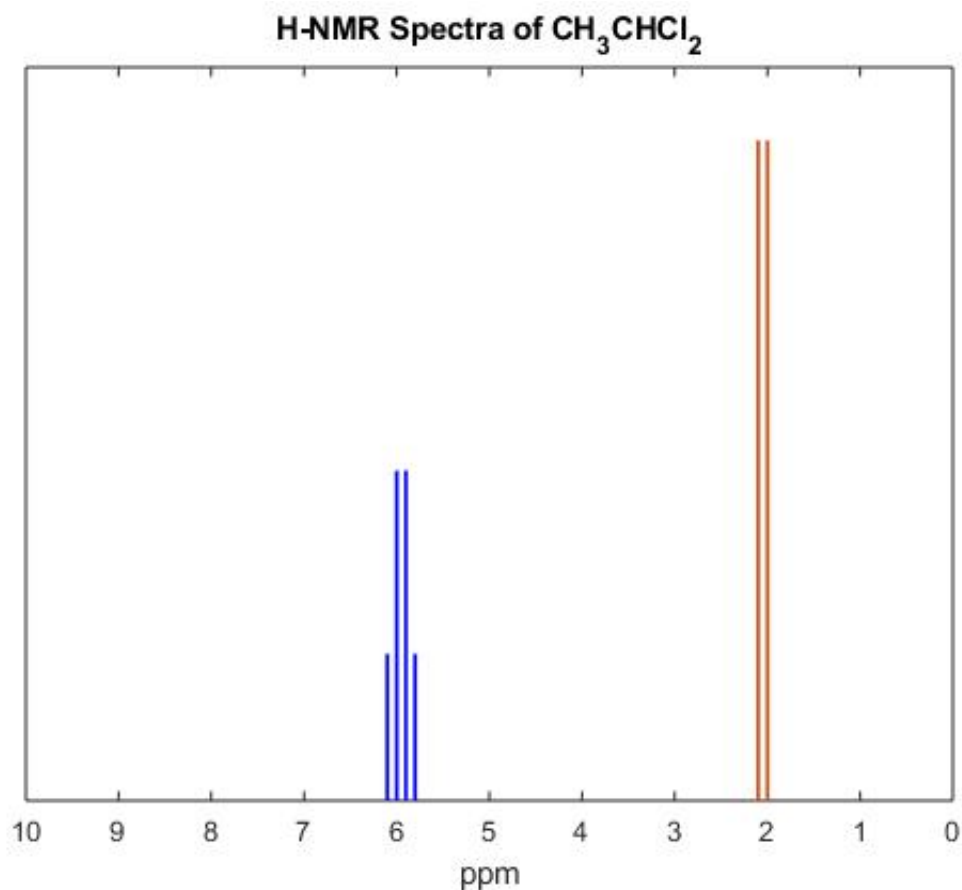


Figure 3.2: H-NMR spectra of di-chloro-ethane

## 3.2 Signal generation and pulse sequences

### 3.2.1 Stimulated Echo Acquisition Mode

STimulated Echo Acquisition Mode (STEAM) is a pulse sequence used for spectroscopy. The technique uses three slice-selective 90-degree radio frequency pulses that are applied simultaneously with three orthogonal gradients. The signal is, thus, derived and localized to the protons in the voxel from the overlapping planes of the three gradients.

The time of appearance of the stimulated echo depends on the spacing of the radio frequency pulses. For instance, if the first two pulses are  $TE/2$  seconds apart then the echo will form at  $TE/2$  seconds after the third pulse.

The time between the second and third pulse is referred as the mixing time and it is typically kept minimum. During this period, the magnetization is stored in the z-plane and therefore does not undergo any T<sub>2</sub> decay. For this reason, the echo time does not include the mixing time

and is simply defined as the sum two time intervals: the time between first and second pulse and the time at which the echo appears after the third pulse i.e.  $TE/2 + TE/2$  which is thus,  $TE$ . Figure 3.3 helps to visualize this.

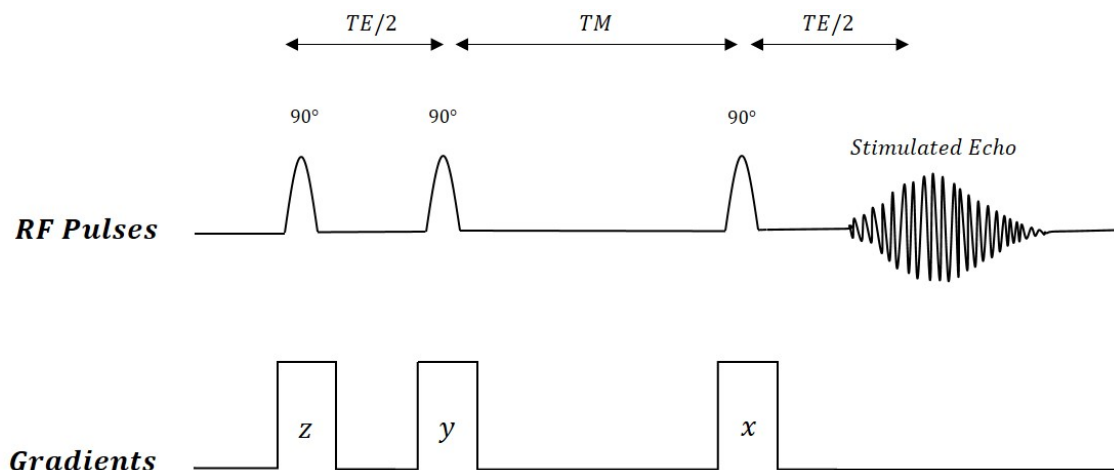


Figure 3.3: A typical STEAM sequence

### 3.2.2 Point Resolved Spectroscopy

The Point RESolved Spectroscopy (PRESS) method is a typical technique used for human spectroscopy. The sequence primarily consists of three slice-selective radio-frequency pulses that are simultaneously applied with three orthogonal gradients, just as in a STEAM sequence. However, the underlying difference is that it employs 90-180-180 degrees pulses instead of the 90-90-90 degrees pulses that are used in a STEAM.

A major limitation of PRESS is the multiple 180 degrees pulses that may put dangerous levels of energy in the system. On the contrary, PRESS is the most commonly used spectroscopic sequence and preferred over STEAM precisely because when energy deposition limits are respected, PRESS yields a higher signal to noise ratio as compared to STEAM. Typically, Specific Absorption Rate (SAR) limits are well respected in protocols so energy absorbed by the tissues is not a point of concern when choosing between PRESS and STEAM.

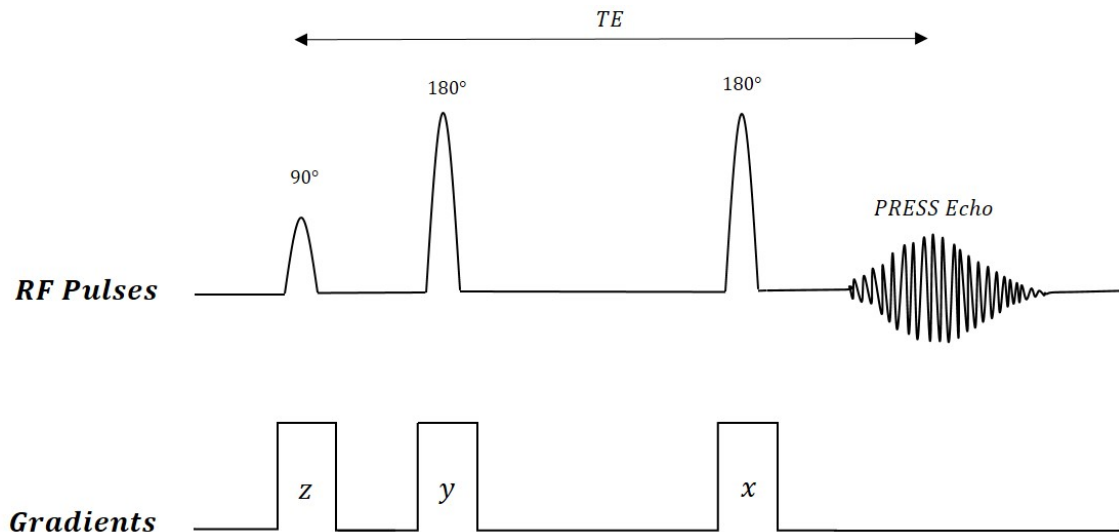


Figure 3.4: A simplified PRESS sequence

### 3.3 Study on Phantoms

Before understanding the “how” of the study regarding phantoms, it is imperative to establish “what” it is that is being studied. Investigation into liver lipid merits an understanding of the liver lipid molecules, essentially triglycerides. Esterification is a process where an alcohol group molecule combines with a carboxylic acid group molecule to form an ester compound. Triglyceride formation is basically esterification where glycerol as an alcohol group containing compound and three fatty acids as carboxylic group containing compounds combine together to form one triglyceride molecule and three water molecules. This is shown in figure 3.5 below.

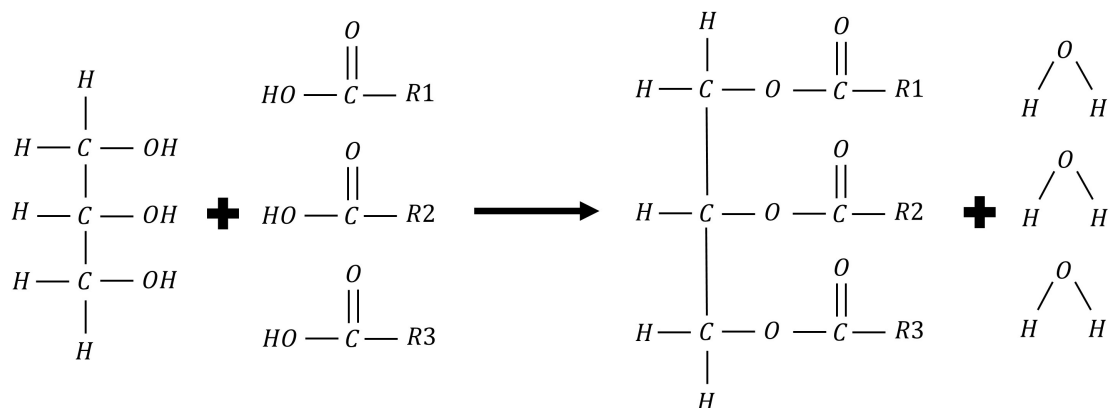


Figure 3.5: Triglyceride formation

The basic hydrocarbon chains R1, R2, R3 are elongated and shown in figure 3.6 which follows the MR spectrum of the molecule in figure 3.7, based on the chemical environment of the respective protons shown in different colors.

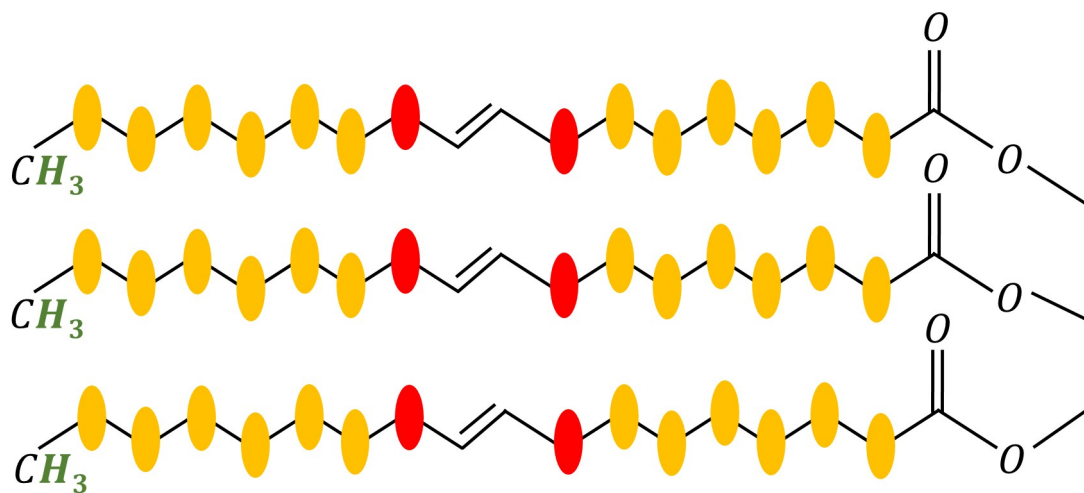


Figure 3.6: Typical triglyceride molecule

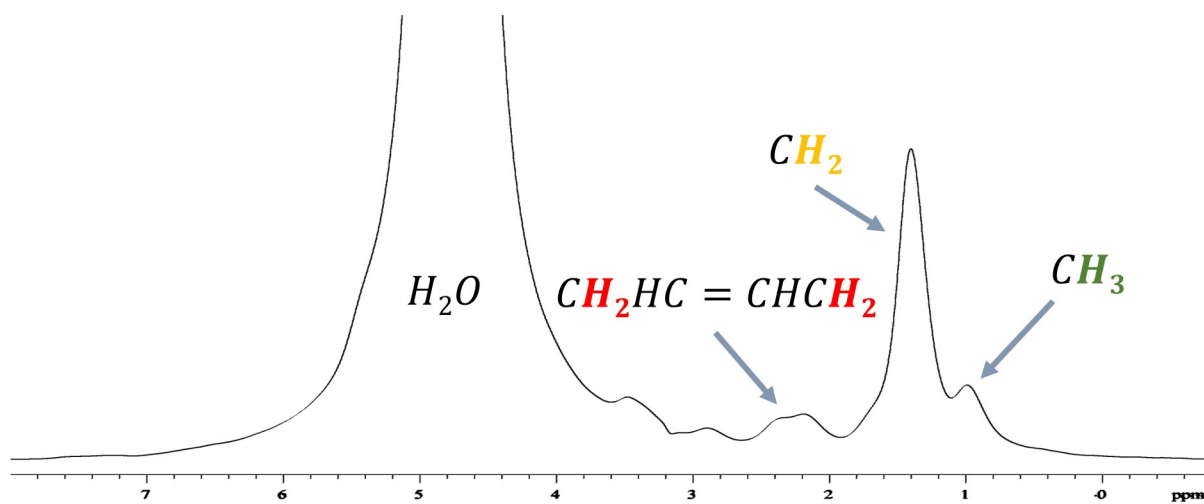


Figure 3.7: NMR Spectrum of a triglyceride molecule

### 3.3.1 Peanut oil and liver lipid

For the phantom construction, peanut oil was chosen to be mixed in a water solution since peanut oil has an NMR spectrum very similar to the protons in the triglyceride molecules in the hepatocellular lipids [28][20][8]. NMR spectra from a peanut oil phantom is shown on the left in figure 3.8 below. The equivalent nature of the two spectra, particularly the occurrence of the individual peaks in the peanut oil spectra, allow it to be used as an alias for the liver lipid for validation tests purposes.

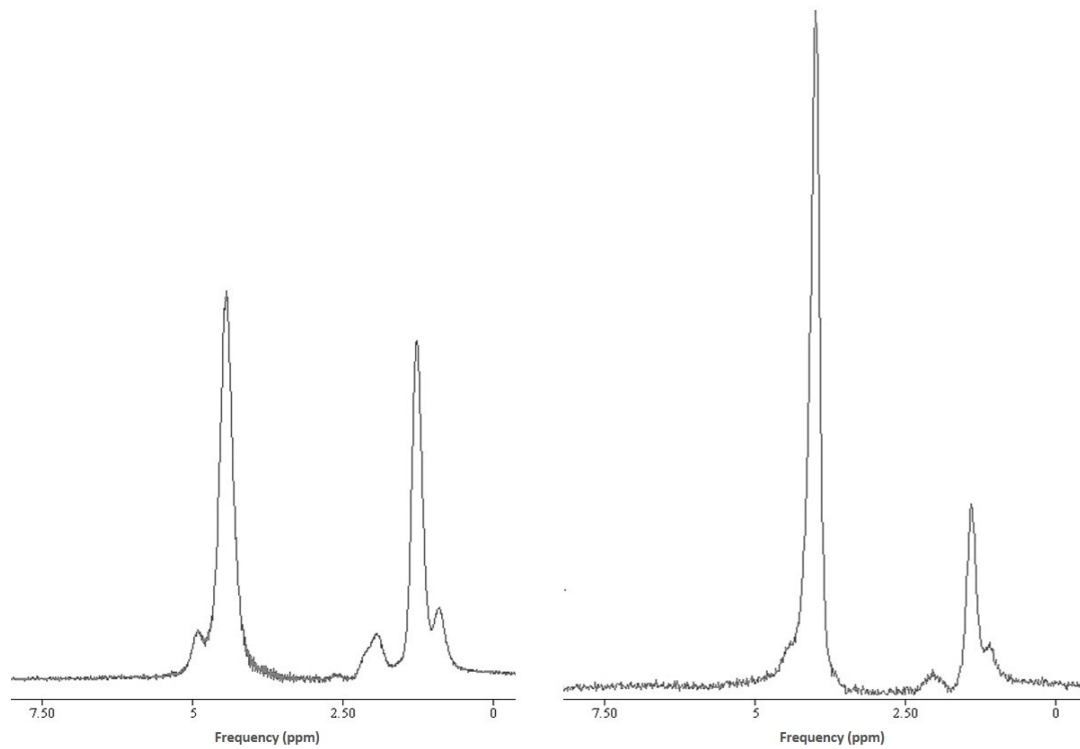


Figure 3.8: NMR spectra of a peanut oil phantom (left) and liver lipid (right)

### 3.3.2 Phantom construction

Fat-Water phantoms were constructed with varying concentrations. The process involved heating distilled water in a beaker on a hot plate. 2% agarose (mass/volume concentration) was added to this distilled water with low heating and stirring until melted using a magnetic stirrer.

43 mmol of Sodium dodecyl sulfate (SDS) (Sigma-Aldrich, St.Louis, MO) was then added to this solution. SDS was added in small quantities at a time to avoid any lumps to be formed in the mixture on addition. SDS is an anionic surfactant and helps to emulsify the oil-water mixture so that a homogenous and stable solution could be made. This followed the addition of 43 mmol sodium chloride which modifies phantoms' dielectric properties [36], 3.75 mmol sodium azide, 0.5 mmol copper (II) sulfate. Finally, known percentages of peanut oil were added to necessary volumes of this solution to make up 50 ml vials. The mixture was thoroughly mixed and allowed to cool.

### 3.3.3 Experimentation and data acquisition on Phantoms

Single voxel spectroscopy (SVS) was performed on both the systems, the 3T and the 7T for the phantoms. Whole body coil was used for excitation on both systems. A 32-channel phased array body/torso coil was used for receive on 3T while a head coil was used on the 7T. The phantoms were housed in a water bath at room temperature, shown in figure 3.9.

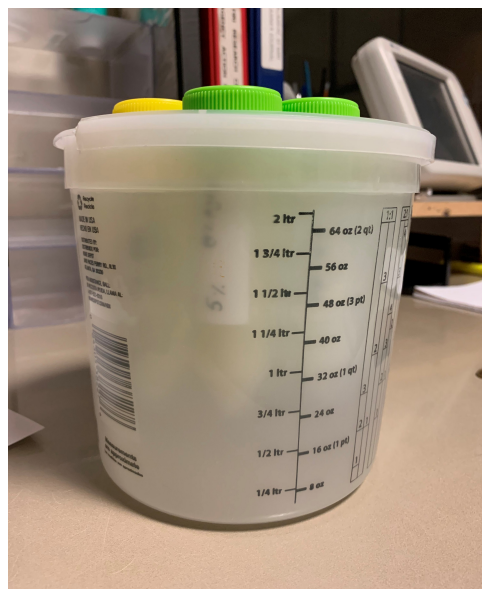


Figure 3.9: Phantoms in Water Bath (room temperature) for scan

Both STEAM and PRESS sequences were used on the phantoms. However, from earlier discussion in section 3.2.2, results from PRESS sequence are of more significance and thus, only these are used for analysis. Figure 3.10 shows a voxel location on one of the vials in the housing setup of the phantoms. The chosen voxel size is 12x12x20 mm. Line widths were



minimized with manual shimming and with an optimized sequence on 3T and 7T, respectively. The green voxels correspond to the shim volumes whereas the white voxels are the volume of interest. Shim volumes are always kept larger than the interested volumes in order to ensure a smooth and homogenous field at and beyond the boundaries of the volume of interest. The TE/TR chosen for the phantoms were 20/5000 ms with 6 averages.

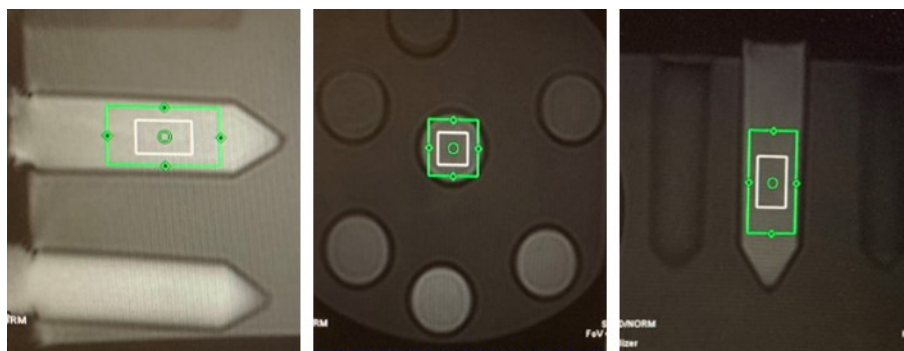


Figure 3.10: Voxel location on a vial in axial, coronal and sagittal planes

### 3.3.4 Phantom data processing

The spectroscopic data was processed in Java-based MR User Interface (jMRUI). The spectra were fit and estimated using the advanced method for accurate, robust and efficient spectral (AMARES) fitting tool in jMRUI. Resonances were resolved using Gaussian line shape. The area under the fitted curve is used for quantification for the respective water and fat peaks. A six peak model was used for the fat peaks estimation, however, some of the fat peaks with very small amplitude were around the same level as the noise floor and thus, were safe to ignore. The two major peaks at 1.3 ppm and 0.9 ppm were therefore, used to evaluate fat fractions in all spectra, using equation 3.1 below. The equation simply sums the area under the fat peaks in the numerator and divides it by the summation of fat and water peaks' areas to compute a fat fraction:

$$FatFraction = \frac{\sum_{i=1}^{FatPeak} A_i}{\sum_{i=1}^{AllPeaks} A_i} * 100 \quad (3.1)$$

### 3.3.5 Phantom results and discussion

Figure 3.11 shows two MR spectra from a scan at 3T; the original and the estimated, processed spectra. The spectra are from the vial with known fat fraction of 25% whereas the registered fat fraction after processing is 24.33%. The fat peak used for estimation is at 1.3 ppm and the water peak is at 4.7 ppm. This is an example where the second dominant fat peak at 0.9 ppm is almost a residual noise and therefore, inevitably ignored.

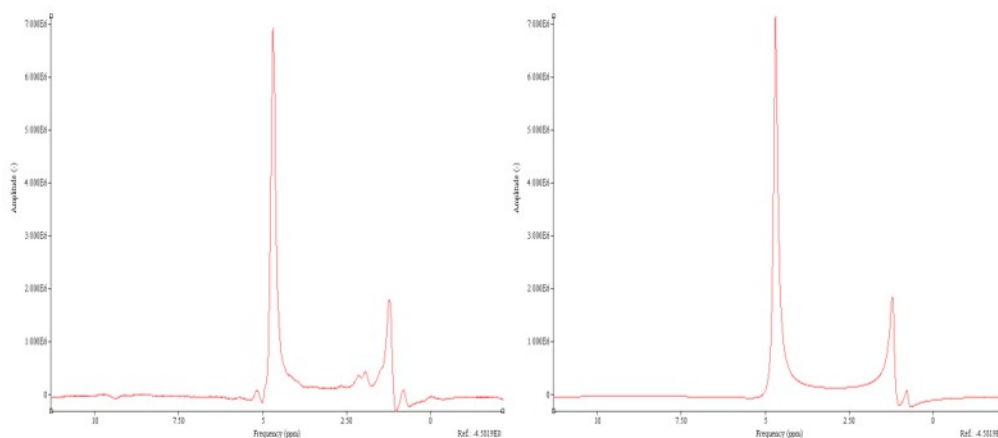


Figure 3.11: Original and an Estimated MR Spectra

Known FF	8	14	18	25	30	40	45	55
MRS 3T	7.34	16.37	16.36	24.33	32.92	41.4	46.19	57.14
MRS 7T	7.5	16.94	18.17	24.84	30.77	37.67	46.61	58.36

Table 3.1: Comparison of Phantom spectroscopy results from 3T and 7T

The results from the 3T and 7T are summarized in table 3.1; all values are in percentages. For all of the phantom on both the scanners, the fat fraction error is less than 10% of the fraction itself which is a good measure of accuracy. Some of the vials such as the 18% for 3T is slightly poor which could be due to the oversimplification of the estimation using only one peak in the fat spectra. These results are better visualized in figure 3.12 below.

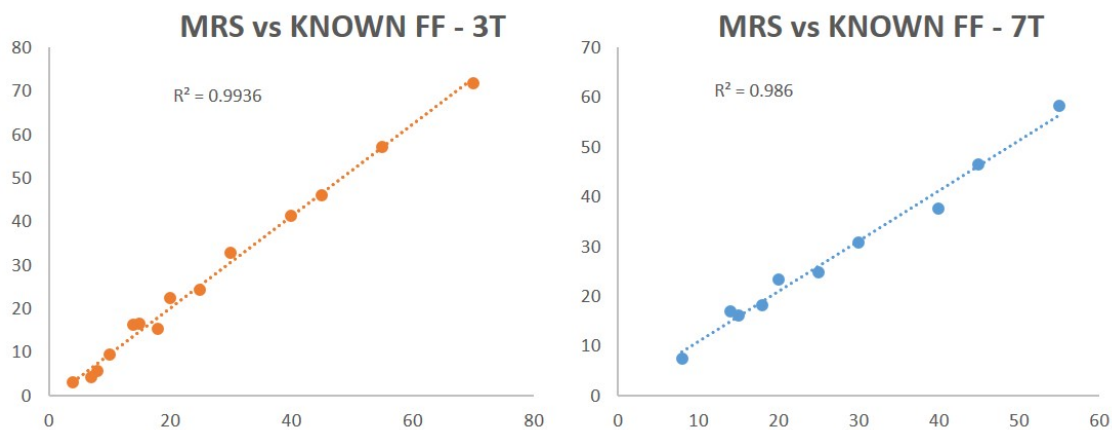


Figure 3.12: Plots showing negligible scatter of measurements from known fat fractions in phantoms

The higher coefficient of determination, 0.995, on the 3T as compared to 0.986 on the 7T suggests the measurements and results on the 3T are more accurate. This could be due to field inhomogeneities at 7T with shimming as a challenge.

The same set of phantoms were scanned by the University of Alabama Birmingham (UAB) with the same protocol. The spectra were processed in the same way with the same estimating parameters. .

Known FF	8	14	18	25	30	40	45	55
MRS 3T UAB	7.24	18.4	16.04	25.9	33.15	37.93	39.46	53.53

Table 3.2: UAB Phantom spectroscopy results from 3T

Table 3.2 summarizes the results from UAB on 3T. The linear regression line and its equation are shown in figure 3.13. The coefficient of determination,  $R^2$  is 0.9661 for UAB 3T measurements and even though this is a good score, it is relatively lower to the measured values at Auburn 3T, nonetheless. The mean error percentage with the scans done at Auburn 3T is 7.71% while that at UAB is 10.76%; both error percentages are fairly low.

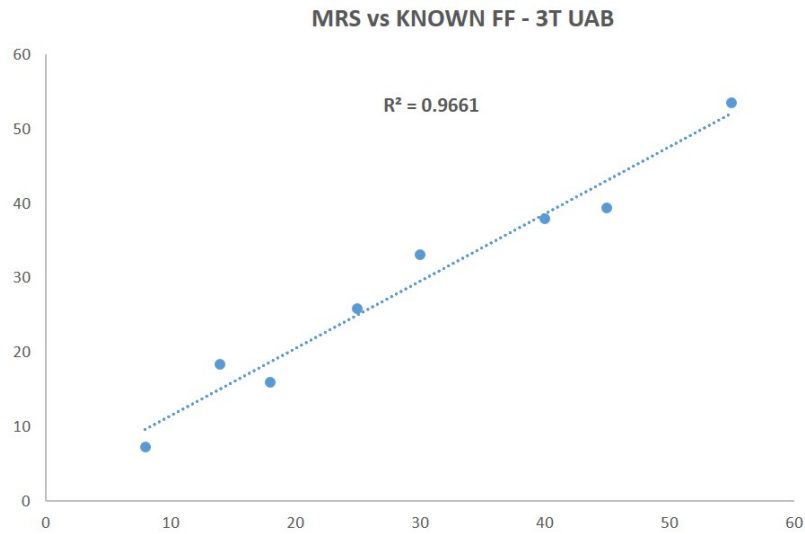


Figure 3.13: Scatter of phantom spectroscopic data scanned at UAB

### 3.4 in-vivo study

The in-vivo study for spectroscopy included measuring the intra-hepatocellular lipid (IHCL) content on fifteen subjects. The primary goal of this study was to set up a robust, accurate and reproducible approach to quantify IHCL. This included some protocol enhancements to reduce the coefficient of variation along with an efficient measurement of T2 of the triglycerides (TG) and correct for that for TG quantification. The study consisted of eight males and seven females, fifteen subjects in total with their body mass indices ranging from 22.2 to 46.7 kg/m<sup>2</sup>.

#### 3.4.1 Protocol enhancements

A single voxel 15x15x15 mm PRESS sequence was used for acquisition. However, some adjustments were made to the standard SIEMENS PRESS sequence in order to optimize it. This optimization assessment was based on the reduction of coefficient of variation (CV). Calculation of CV comprised of registering measured lipid content three times on each volunteer and evaluating mean and standard deviation to calculate CV for each protocol adjustment. Equation 3.2 shows CV is essentially a ratio of standard deviation and mean for a measured entity which in this case is the registered lipid content.

$$CV = \frac{\sigma}{\mu} \quad (3.2)$$

where  $\sigma$  is the standard deviation of the measured values and  $\mu$  is their mean.

In-vivo scans are always subject to respiratory motion. Although respiratory motion can be very little around the liver, it is significant when the voxel sizes are as small as  $15 \text{ mm}^3$ . Literature suggests liver lipid content is non-uniform around the liver, this is further investigated along with T2-correction later in the section. Figure 3.14 below shows an axial and coronal view of the liver with three different voxel positions suggesting a significant difference in fat fraction. Therefore, a breath-held scan is preferred to ensure that the voxel location for acquisition is indeed the one that is imaged and is not disturbed due to the respiratory motion. This requires setting up localizer scans with breath-holds as well.

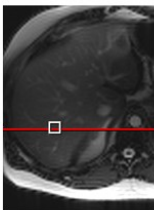
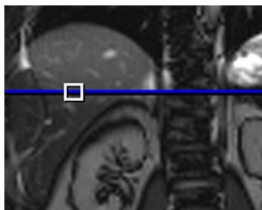
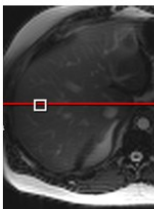
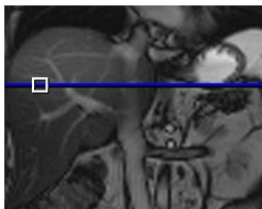
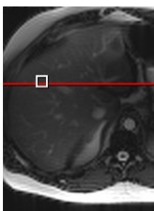
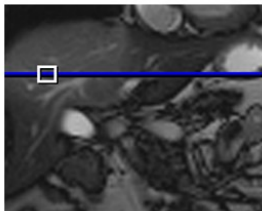
Fat Fraction %	Orientation	
	Axial	Coronal
23.25		
22.07		
17.26		

Figure 3.14: Three different voxels on the liver showing non-uniform lipid content

Although the breath-hold scan time is very small, approximately fifteen seconds on average, it is preferable to use a scheme such as a navigator guided Prospective Acquisition Correction (PACE) that would acquire data at particular respiratory phases, thus, eliminating the need for a breath-hold altogether. For an imaging modality (discussed in the following chapter), parallel imaging schemes with compressed sensing are available to allow for free-breathing acquisition [3].

Table 3.3 shows that the coefficient of variation reduced by about 5% when the echo time was reduced from 30ms to 24ms. This is attributed to greater signal to noise because the spins get a relatively lesser time to dephase out and lose magnetization and hence the recorded signal is stronger.

Optimized sequence breath-hold and free-breathing (n=27)		
TE	30,35,40,50	24,30,35,50
CV	12.8%	7.2%

Table 3.3: 5% CV improvement with shorter echo times

A comparison of a standard SIEMENS sequence with free-breathing against a breath-hold acquisition and an acquisition with the PACE mechanism is shown in table 3.4. The two mechanisms, breath-held and with PACE, amongst themselves did not show a significant improvement but were 4% better in terms of CV than the free-breathing protocol.

Acquisitoin: PRESS, 15mm <sup>3</sup> voxel on liver left lobe			
Sequence	SIEMENS	Opt. /w breath-hold	Opt. /w PACE
TEs	30,35,40,50	30,35,40,50	30,35,40,50
CV	16.9% (n=14)	12.6% (n=13)	13% (n=14)

Table 3.4: 4% CV improvement on the standard SIEMENS sequence with optimized breath-hold and PACE

### 3.4.2 T2 Correction

Furthermore, using additional TEs for T2 correction further reduced the CV by 2%. This is summarized in table 3.5 where it can be seen that the CV reduced from 8.7% for a 2-TE protocol to 6.7% for a 5-TE protocol.

Optimized sequence breath-hold and PACE with multiple TEs				
#TEs	2-TE	3-TE	4-TE	5-TE
TEs	24,50	24,30,50	24,30,35,50	24,30,35,40,50
CV	8.7%	7.4%	7.2%	6.7%

Table 3.5: 2% CV improvement with multiple TEs for T2 correction

All echo times in the tables are in milliseconds. Mono-exponential fitting of the spectroscopy data acquired at 5 echo-times was done for both: lipid and water peaks. This exponential fitting allowed for an extrapolation to time point zero or  $TE = 0$ . This is the point where lipid and water signal amplitudes are used for the computation of fat fraction.

Figures 3.15, 3.16, 3.17 show T2-corrections for three different voxels on volunteer 7 in this study. It is evident from the figures below that the signal decay by water is greater than that by lipid which is why water typically has a lower T2 relaxation time than lipid.

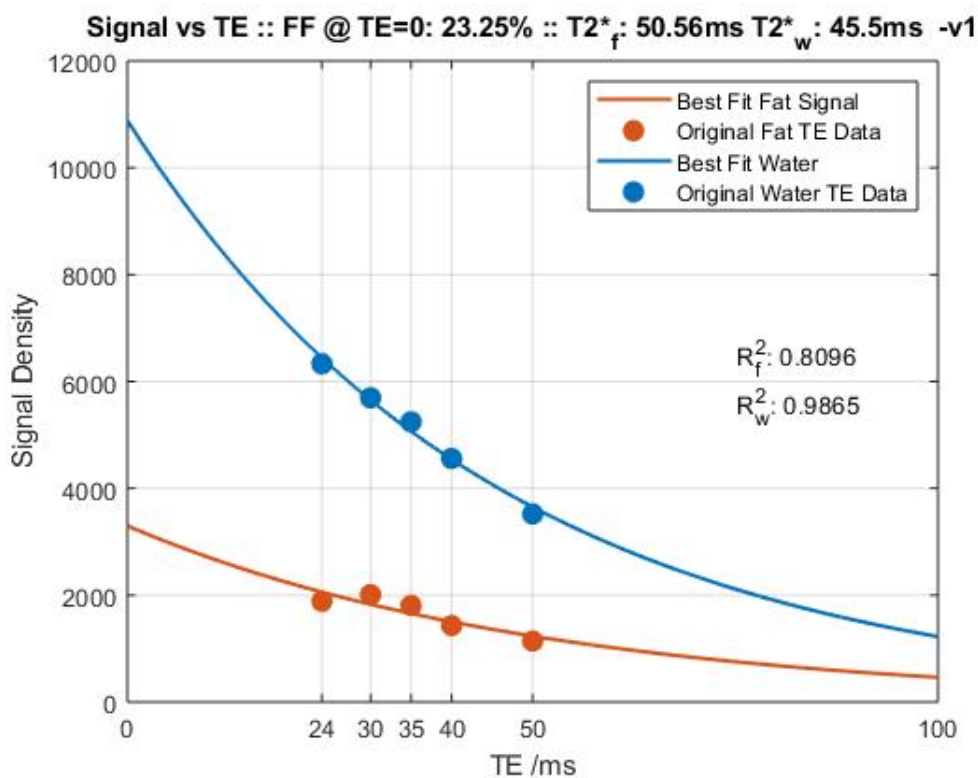


Figure 3.15: T2 Correction on voxel 1 of volunteer 7

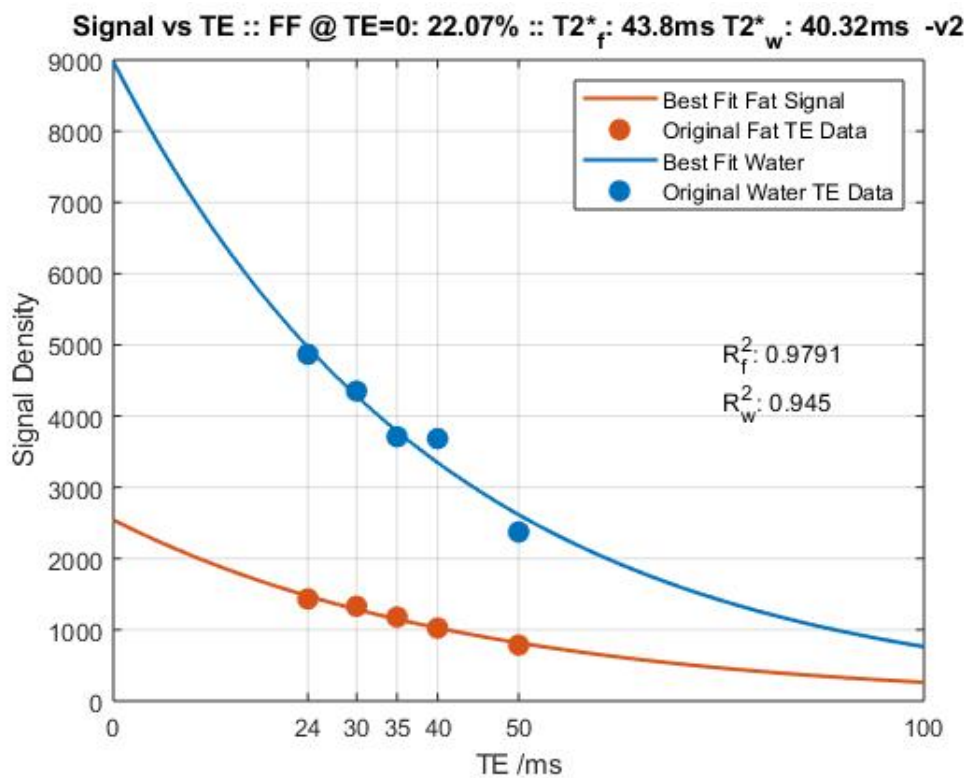


Figure 3.16: T2 Correction on voxel 2 of volunteer 7



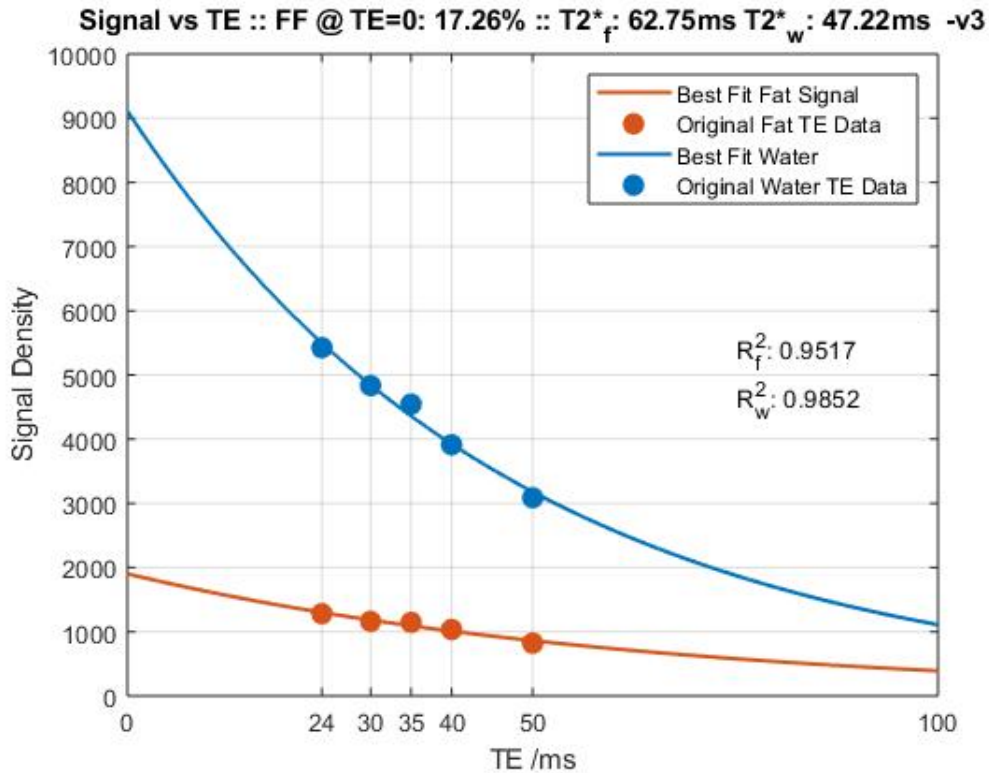


Figure 3.17: T2 Correction on voxel 3 of volunteer 7

Table 3.6 shows fat fraction values for all subjects at five echo times in milliseconds. These are in %. The mean  $\mu$  and standard deviation  $\sigma$  of these fat fraction percentages are also shown, followed by a column showing T2-corrected fat fraction % which is labeled as “T2” in the table. Next to it is the error %  $\Delta$  between the mean  $\mu$  fat fraction and the T2-corrected fat fraction percentages, computed simply as  $\Delta\% = (\mu - T2)/T2 * 100$ . A mean of the T2-corrected fat fractions of the three voxels  $\mu_{T2}$  and the standard deviation of the T2-corrected fat fraction of these three voxels  $\sigma_{T2}$  is also shown in table 3.6.

On average, standard deviation of all 15 volunteers (not shown in table) is 3.01% in the three voxels which is not too significant primarily for two reasons: one, since there are a lot of measurements involved towards the quantification, any error may propagate and manifest in this 3.01% value and two, it is quite possible to end up choosing one or more voxels that may have a part of vessel or duct in them, resulting in biased signal which would translate into this 3.01%. Therefore, this 3.01% standard deviation amongst three voxels is not a conclusive evidence of non-uniformity in liver lipid content, however, it does indicate some non-uniformity

and warrants the need to carefully place the voxels, rendering the study more or less, operator dependent.

Furthermore, table 3.6 suggests that average fat fraction error % is 13.17%. This error % in fat fraction is between uncorrected and T2 corrected fat fractions in all voxels of all subjects. This 13.17% error % is important since it is an error % and thus, suggests that higher the fat fraction value, greater the deviation from the true fat fraction value. On very small fat fractions, this would be insignificant.

#	TE	24	30	35	40	50	$\mu$	$\sigma$	T2	$\Delta$	$\mu$ T2	$\sigma$ T2
1	v1	38.94	38.08	35.30	35.45	36.09	36.77	01.64	42.94	14.36	39.34	03.12
	v2	36.06	37.28	38.37	31.36	37.64	36.14	02.80	37.73	04.21		
	v3	35.21	35.10	34.78	32.72	33.87	34.34	01.05	37.35	08.07		
2	v1	50.35	53.07	54.16	53.12	58.32	53.80	02.89	44.97	19.64	44.05	01.90
	v2	46.42	49.82	50.21	50.85	53.01	50.06	02.38	41.86	19.59		
	v3	44.27	47.61	49.47	48.64	43.21	46.64	02.75	45.31	02.94		
3	v1	39.64	36.94	38.73	38.87	37.17	38.27	01.16	40.34	05.13	36.05	04.01
	v2	37.41	39.76	39.40	38.81	41.11	39.30	01.35	35.42	10.95		
	v3	33.89	35.80	35.20	35.33	36.40	35.32	00.93	32.39	09.06		
4	v1	33.68	34.16	32.80	32.89	34.77	33.66	00.84	33.63	00.09	29.78	03.39
	v2	28.85	28.92	26.92	28.17	31.79	28.93	01.79	27.25	06.17		
	v3	29.51	31.15	30.47	28.83	32.59	30.51	01.46	28.47	07.17		
5	v1	34.76	34.21	32.71	30.63	33.19	33.10	01.60	37.99	12.87	35.58	02.12
	v2	33.90	33.43	33.72	32.54	34.37	33.59	00.68	33.99	01.17		
	v3	31.54	31.46	31.27	28.60	29.19	30.41	01.40	34.75	12.48		
6	v1	55.06	56.81	56.66	59.02	51.64	55.84	02.74	55.56	00.50	47.96	06.73
	v2	50.64	53.44	54.56	54.90	56.92	54.09	02.30	45.54	18.78		
	v3	48.64	53.41	54.12	54.62	56.80	53.52	03.01	42.77	25.13		
7	v1	22.95	26.09	25.62	23.89	24.48	24.61	01.27	23.25	05.83	20.86	03.17
	v2	22.74	23.41	24.12	21.75	24.87	23.38	01.21	22.07	05.93		
	v3	19.10	19.38	20.13	20.90	21.01	20.10	00.86	17.26	16.48		
8	v1	11.00	12.47	13.71	11.91	13.71	12.56	01.17	09.63	30.43	09.57	01.30
	v2	09.58	10.87	11.01	10.46	11.76	10.74	00.80	08.25	30.13		
	v3	11.09	11.42	12.34	11.95	11.29	11.62	00.51	10.84	07.18		
9	v1	42.11	42.50	44.45	44.74	43.62	43.48	01.16	39.84	09.15	38.63	07.47
	v2	45.83	45.92	44.66	46.53	46.21	45.83	00.71	45.43	00.88		
	v3	42.43	45.23	45.21	45.16	48.04	45.21	01.98	30.63	47.61		
10	v1	07.95	11.08	08.65	08.62	08.69	09.00	01.20	08.59	04.75	07.30	01.13
	v2	07.78	08.62	09.31	09.07	09.18	08.79	00.62	06.82	28.91		
	v3	06.79	08.22	07.67	08.54	07.39	07.72	00.69	06.50	18.80		
11	v1	17.51	16.80	18.11	17.12	18.03	17.51	00.57	16.89	03.69	15.77	01.45
	v2	16.79	19.87	17.04	18.53	18.86	18.22	01.29	16.29	11.84		
	v3	16.20	17.31	17.77	18.11	18.93	17.66	01.01	14.13	25.01		
12	v1	15.23	15.29	15.72	17.27	16.61	16.02	00.89	13.47	18.96	13.62	01.37
	v2	16.72	18.07	17.32	18.25	19.25	17.92	00.96	15.06	19.00		
	v3	13.00	14.49	13.44	14.66	14.10	13.94	00.70	12.34	12.95		
13	v1	48.15	47.15	46.78	47.17	49.20	47.69	00.99	47.52	00.36	45.88	01.48
	v2	48.09	46.01	48.29	48.37	50.15	48.18	01.47	45.46	05.99		
	v3	47.73	48.75	49.33	48.69	51.91	49.28	01.58	44.66	10.35		
14	v1	28.43	32.72	30.46	31.93	30.17	30.74	01.66	28.01	09.75	24.83	04.10
	v2	23.92	28.63	26.78	28.62	30.69	27.73	02.54	20.20	37.27		
	v3	26.58	28.74	27.88	26.74	28.33	27.65	00.96	26.29	05.19		
15	v1	09.44	11.33	09.32	08.78	09.88	09.75	00.97	10.47	06.88	09.26	02.44
	v2	11.28	12.66	13.10	14.33	11.04	12.48	01.36	10.87	14.83		
	v3	07.04	08.72	08.38	07.47	09.04	08.13	00.85	06.45	26.05		

Table 3.6: MRS Fat Fractions data summary

Subject#	T2 Lipid (ms)	T2 Water (ms)
1	36.71	43.04
2	50.31	38.02
3	39.06	36.58
4	39.22	36.78
5	33.26	38.34
6	43.97	32.14
7	52.37	44.35
8	61.58	44.73
9	48.10	35.42
10	53.61	42.43
11	47.07	39.52
12	49.84	39.62
13	37.36	33.99
14	45.76	36.48
15	45.77	39.02
$\mu \pm \sigma$	$45.60 \pm 7.56$	$38.70 \pm 3.71$

Table 3.7: T2 of Lipid and Water in-vivo

Table 3.7 shows averaged T2 values of all three voxels for each subject. A mean and standard deviation of these T2 values is then shown in the last row. Water decays faster than the lipid and a shorter T2 value for water confirms this.

## Chapter 4

### Lipid quantification with MR Imaging

#### 4.1 Evolution of MR Imaging approaches

The earliest proposition on fat water separation techniques traces back to Dixon who proposed the famous two-point method [35]. The concept is based on the acquisition of two images: the in-phase one and out-of-phase one. The in-phase refers to the point where the phases of fat and water are aligned and the out-of-phase refers to the first time the two phases are entirely opposed. The voxel brightness reflects the added magnetization of the chemical components in the transverse plane, for the in-phase image whereas for the out-of-phase image, the voxels represent the difference between water and fat magnetizations [6]. A simplistic model where signal is a function of time shift is given in equation 4.1. It leads to the classical conclusion that the water-only image is the addition of the in-phase and out-of-phase images whereas the fat-only image is the subtraction of the in-phase and out-of-phase images.

$$y(t) = W + Fe^{i\omega't} \quad (4.1)$$

where water and fat are represented by  $W$  and  $F$  respectively and  $\omega' = \gamma B\delta$ , wherein  $\gamma$  is the gyromagnetic ratio,  $B$  is magnetic field and  $\delta$  is the difference in fat and water resonant frequencies.  $\omega'$  is known a-priori.

With the knowledge of  $\gamma$  and using this model, in-phase and out-of-phase echo times can be known and thus, images can be acquired using those times, leading to voxel by voxel separation of water and fat:

$$2W = y_{IP} + y_{OP} \quad (4.2)$$

$$2F = y_{IP} - y_{OP}$$

The basic issue with this model is the assumption of no field inhomogeneity in data acquisition, thus leading to phase errors. Literature therefore covers modifications to acquisition strategies, accuracy of signal modeling and algorithms to correct for static field inhomogeneity and accounting for these phase errors [33]. A flexibility in the choice of echo times in the 2-point Dixon scheme was proposed by Eggers et. al. [12]. More often than not, these images present leakages of fat into water images and vice versa as shown in figure below:

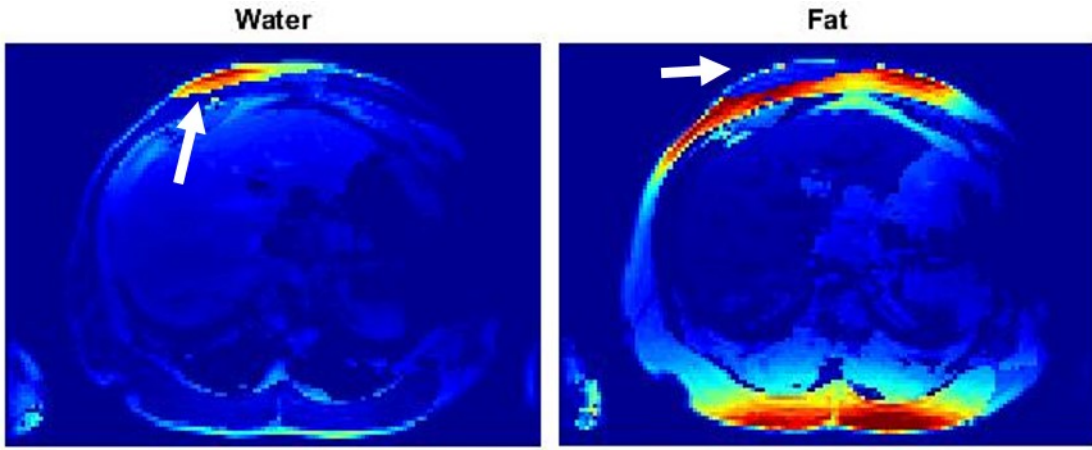


Figure 4.1: Leakage of fat signal in water image and vice versa

Including off-resonance effects into the signal model, leads to equation 4.3

$$y(t) = (W + Fe^{i\omega't})e^{i\omega t} \quad (4.3)$$

where  $\omega$  is not known a priori. It is spatially varying and encompassing phase errors due to field inhomogeneities. The original Dixon method takes an absolute value and thus, removes this term [5] [35]. Estimating  $\omega$  for each pixel results in the formation of a field map along with the estimation of fat and water. The estimation is simplified if echo times are increased to 3 or more. A 3-point Dixon approach (using three echoes hence the name 3-point) was first introduced by Kim et al and was generalized by Glover to a  $(-\Delta T, 0, \Delta T)$  and further by Xiang

to  $(t_0, t_0+\Delta T, t_0+2\Delta T)$  for arbitrary  $t_0$  and  $\Delta T$  [13][37]. Finally, Reeder et al. provided a general solution for all arbitrary time shifts.

There are many algorithms that present the water and fat estimations with different schemes, for instance, constraining the initial phase to be the same for water and fat at certain echo times helps to reduce the number of estimated parameters and simplifies the estimation problem [9]. The 2-point as well as the 3-point Dixon techniques have some limitations nonetheless, for instance, the field variation is held within a restricted range and does not account for large field inhomogeneities [26][10]. A popular way to address this is to model the equation in a maximum likelihood setup where unknown parameters are estimated with a least squares approach by minimizing the error between the model and the measured data iteratively for each voxel. Reeder et al. proposed such a scheme called Iterative Decomposition of Water and Fat with Echo Asymmetry and Least-squares estimation [29].

Equation 4.3 assumes a single resonant peak for each of the two identities: water and fat. While this is true for water it is not the case for fat. There are at least six identifiable fat peaks in the human liver at 3T and thus it is critical for an accurate estimation to account for them to prevent errors in the quantification [30] [11]. Yu et al. proposed a signal model that accounts for multiple fat peaks, shown in equation 4.4 below [41]:

$$y(t) = (W + F \sum_{m=1}^M \alpha_m e^{i\omega_m t}) e^{i2\pi\psi' t} \quad (4.4)$$

where fat peaks  $M$  are weighted with  $\alpha_m$  and normalized to add to unity.  $\omega_m$  and  $\alpha_m$  are known apriori and are common for all voxels so they do not increase the number of unknowns, however, the complexity of the algorithm is somewhat increased as  $t$  encapsulates time for each echo and  $\psi'$  modeling a complex field map.

The IDEAL approach greatly helps to estimate fat, water as well as field map. It entails choosing an initial guess for the field map, thereby linearizing the problem and iteratively resolving the equation via matrix operations until the fitting error locally converges. The signal model is reformulated as equation 4.5

$$s(r, t_n) = [\rho_w(r) + \rho_f(r)] \sum_{i=1}^M \alpha_i e^{i2\pi\delta_i t_n} e^{-\gamma(r)t_n}, \quad n = 1, \dots, N \quad (4.5)$$

where  $\rho_w$  and  $\rho_f$  are complex with spatial location  $r = (x, y)$ ,  $\delta_i$  is the chemical shift of the  $i^{th}$  fat peak,  $\alpha_i$  its relative weight and  $\gamma(r) = 1/T_2^* - i2\pi f(r)$  with  $f(r)$  being the local frequency shift due to field inhomogeneity. Equation 4.5 can be written in a matrix form

$$A_\gamma g = s \quad (4.6)$$

$$\begin{pmatrix} e^{-\gamma t_1} & e^{-\gamma t_1} \sum_{i=1}^M \alpha_i e^{i2\pi\delta_i t_1} \\ \dots & \dots \\ e^{-\gamma t_n} & e^{-\gamma t_n} \sum_{i=1}^M \alpha_i e^{i2\pi\delta_i t_n} \end{pmatrix} \begin{pmatrix} \rho_w \\ \rho_f \end{pmatrix} = \begin{pmatrix} s(1) \\ \dots \\ s(N) \end{pmatrix} \quad (4.7)$$

and resolved as a least square error minimization problem shown in equation 4.8

$$\rho_w, \rho_f, \gamma = \arg \min_{\rho_w, \rho_f, \gamma} \|A_\gamma g - s\|^2 \quad (4.8)$$

IDEAL can use complex values and arbitrary fat peaks and more than three echoes, however, the convergence to a local minimum can sometimes result in fat and water swaps. Typically, six echoes are acquired. One of the many reasons for artifacts in images that cause inaccurate fat quantification is phase errors which can be reduced by eliminating the phase information altogether at the time of fitting, however, that limits the fat fraction range to only 0-50% [41][30]. A mixed magnitude/complex fitting approach that includes discarding the phase of the first echo only and using the rest of the complex images for the least-squares fitting is hence a better approach for a more dynamic 0-100% fat fraction range [17]. Yu et. al. argue that this first echo's phase is corrupted since the prewinder gradient preceding the first read-out gradient is different from the fly-back gradient preceding the read-out gradient of other echoes, thus causing eddy current inconsistencies [42]. A removal of noise bias can then be used on these fitted images by computing the fat fraction as



$$\zeta = \frac{\delta_{fat}}{\delta_{fat} + \delta_{water}} \quad (4.9)$$

for fat dominant pixels whereas for water dominant pixels, since water signal is stronger, the following equation can be used to evaluate water fraction first and subtracting that from the total signal, thus reducing noise-based errors at low fat fractions[25].

$$\zeta = 1 - \frac{\delta_{water}}{\delta_{fat} + \delta_{water}} \quad (4.10)$$

Yu et. al. proposed a version of IDEAL wherein the multi-echo data is down-sampled and passed through a binary mask and used as a low-resolution initial estimate of the field map [40]. Each pixel in this low-resolution image is representing a group of pixels in the high-resolution image, thus referred in the text as super-pixels. Super-pixel with median field map value and super-pixels closest to it form a neighborhood, from which the one spatially closest to the center of mass is chosen as the starting super-pixel. Pixels corresponding to this starting super-pixel are first iteratively estimated with an initial guess, which is the low-resolution field map. Rest of the field map is evaluated in a square spiral trajectory. The initial guess for each new pixel for the rest of the field map is a local 2D linear extrapolation from the preceding estimated pixels [40]. Thus, Yu's region growing algorithm exploits correlation between neighboring pixels with a critical starting point for iteration to begin the estimation that then grows within the field map image, hence the name region growing algorithm. Berglund et al also proposed a similar scheme, however, it included multiple starting or seed points at different regions of the field map image [4]. An improved version of it for phase correction was proposed by Ma et al [23]. Almost all morphological methods derive an estimate from low-resolution images to guide a region-based approach involving thresholding and iteration initialization in order to estimate the high-resolution field map from these low-resolution sets.

A robust approach for the efficient separation of water and fat is Hernando's graph-cut algorithm. Hernando et. al. [19] obtains the maximum likelihood of the signal model by minimizing the cost function. Minimizing voxel by voxel is undesirable due to multiple local

and global minimizers and sensitivity to noise. Thus, minimization is jointly done for all pixels  $q=1, \dots, Q$  [18].

$$\rho_w, \rho_f, f_B = \arg \min_{\rho_w, \rho_f \in C^Q, f_B \in R^Q} \sum_{q=1}^Q R_0(\rho_w, \rho_f, f_B, q : s_q) + \mu \sum_{q=1}^Q \sum_{j \in \delta_q} w_{q,j} V(f_{B,q}, f_{B,j}) \quad (4.11)$$

wherein  $\delta_q$  is the minimum neighborhood of the voxel  $q$ ,  $\mu$  is a regularization parameter which balances the data consistency and smoothness of the solution which is what makes this approach different from others.  $w_{q,j}$  are spatially dependent weights and  $V(f_{B,q}, f_{B,j})$  penalizes the roughness of the field map. Similar scheme was used by Huh et. al. where they introduced a penalized likelihood parameter to control the regularization of the field map [21].

The use of variable projection (VARPRO) for dimensionality reduction allows isolation of the field map term from the equation and thus it is estimated first. This is then followed by solving linear problems for fat and water at each voxel. Solving for the field map is still challenging as gradient-based methods typically converge to a suboptimal solution. Hernando et al overcomes this limitation by discretizing the problem and mapping it to a graph-cut problem in order to solve with only a sequence of binary decisions at each iteration [19].

A graph-search approach is typically used to transform a discrete image volume into a multi-column graph space where every voxel in the original volume corresponds to a node in the graph, connected by various edges, thus, constituting a surface with possible prior constraints within graph connectivity [10]. The solutions of such problems provide estimations of globally optimal resultant surfaces (GOOSE).

Compared to Hernando et al's graph cut algorithm, Cui et al's GOOSE relies on constraints to enforce smoothness of the field map by limiting differences in adjacent field map voxels to a small range. The discretization of this problem is a graph optimization problem wherein each vortex of the graph is constrained to be connected to a small number of neighbors. The problem can then be directly estimated using a surface segmentation algorithm [24]. Such a non-iterative solution is guaranteed to converge to a global minimum of the constrained optimization problem [10].

## 4.2 Phantom Experimentation

The study used Fast Low Angle SHot (FLASH) sequences to acquire data on 3T Siemens scanner. The same phantoms used for spectroscopy in this thesis were used for imaging as well. FLASH sequence is essentially repetitive gradient echo signal with low flip angles. Spoiler gradients are used after each echo to spoil any remaining transverse magnetization. Since very short TR is possible, good T1 contrast is achievable as reasonable signal level is retained.

Although, the scanner spits out the separated fat, water and fat fraction DICOM images, the acquired raw data was still processed with different fat/water separation schemes (discussed in earlier sections) to generate the fat, water and fat fraction images in order to verify if the images were in agreement with the scanners processed results, if not any better.

The acquisition was done with 6 echo times with minimum possible TE optimization on a FLASH 3D sequence. 20 slices were acquired in the coronal plane to have a pool of slices to choose a representative slice from. One representative slice was chosen and processed to evaluate fat fraction. The separated water and fat images are shown in figure 4.2a and 4.2b respectively. Figure 4.2c shows region of interests in yellow circles with evaluated fat fractions. Figure 4.2d shows the known fat fraction values of the peanut-oil phantoms. All fat and water separation along with complex fitting is done using Hernando et. al's approach [19] [17]; use of the fat-water toolbox is herein, sincerely acknowledged [34].

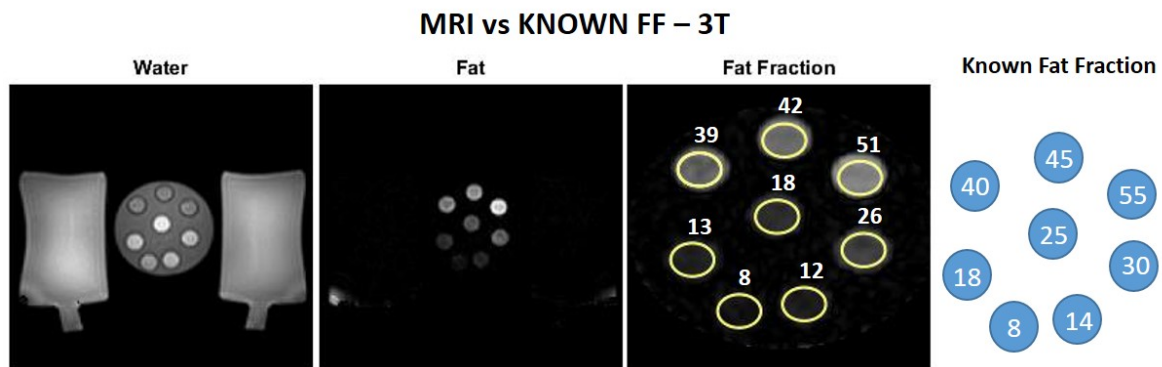


Figure 4.2: Fat Fraction on Phantoms at 3T

Table 4.1 summarizes the results from the imaging and the spectroscopy with percentage error on each vial. This reflects that an average error percentage is lower in spectroscopy than

imaging, which is expected as spectroscopy is considered the non-invasive gold standard for lipid quantification [7][22][38].

Known %	8	14	18	25	30	40	45	55	Mean
MRS 3T	7.34	16.37	16.36	24.33	32.92	41.4	46.19	57.14	-
MRS Error%	8.25	16.93	9.11	2.68	9.73	3.5	2.64	3.89	7.09
MRI 3T	7.89	12.13	13.42	18.53	26.33	39.01	42.76	51.72	-
MRI Error%	1.38	13.36	25.44	25.88	12.23	2.48	4.98	5.96	11.46

Table 4.1: Comparison of MR Spectroscopy with MR Imaging on Phantoms

### 4.3 in-vivo study

Data from four institutions was collected for this study: Auburn University (AU), University of Alabama at Birmingham (UAB), Pennington University (PU) and University of Mississippi (UM). The main purpose of the study was to ensure that similar if not identical protocols were run to acquire data and then different data is processed using the same post-processing techniques. In cases where it was not possible due to a different vendor such as Siemens for Auburn University and General Electric for Pennington University, parameters used were kept as similar as possible.

Institute	FA /°	Slices	Sl.Th.	TR	TE1	TE2	TE3	TE4	TE5	TE6
PU	3	12	5	7.97	1.13	2.11	3.08	4.06	5.03	6.00
UM	5	36	4	9.00	1.25	2.50	3.75	5.00	6.25	7.5
UAB	9	96	3	3.97	1.23	2.46	-	-	-	-
AU (1)	5	20	4	9.00	1.24	2.47	3.70	4.94	6.16	7.39
AU (2)	5	24	3	9.00	1.24	2.47	3.70	4.94	6.17	7.39
AU (3)	5	20	4	7.49	1.24	2.47	3.74	4.99	6.24	7.39

Table 4.2: Protocol summary for multi-site liver fat fraction study

Table 4.2 presents a summary of acquisition protocol for multi-site liver fat fraction study. FA refers to flip angle in degrees, Sl.Th. is slice thickness in millimeters while TR and TE are

repetition time and echo time in milliseconds, respectively. Results from these six datasets are shown in the following six figures.

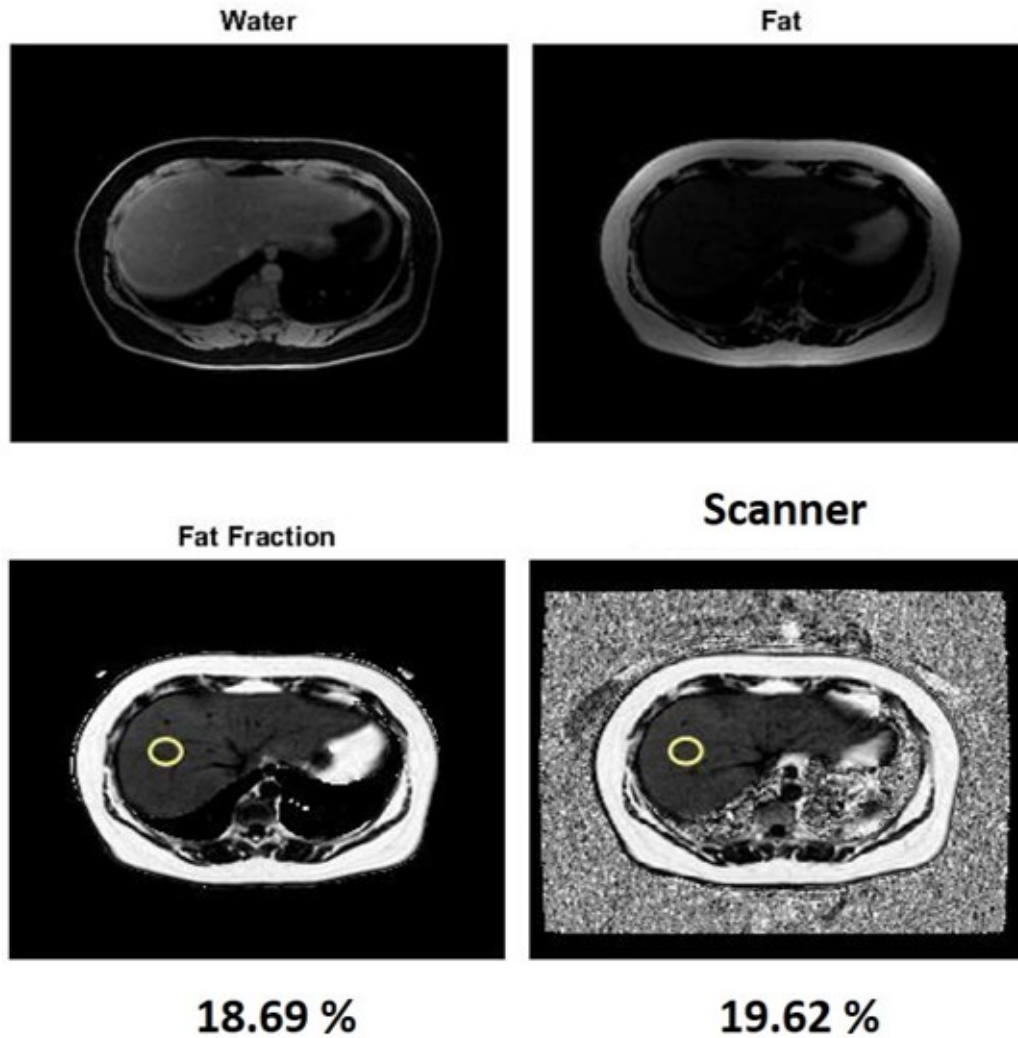


Figure 4.3: Pennington University - Liver Fat Fraction 3T

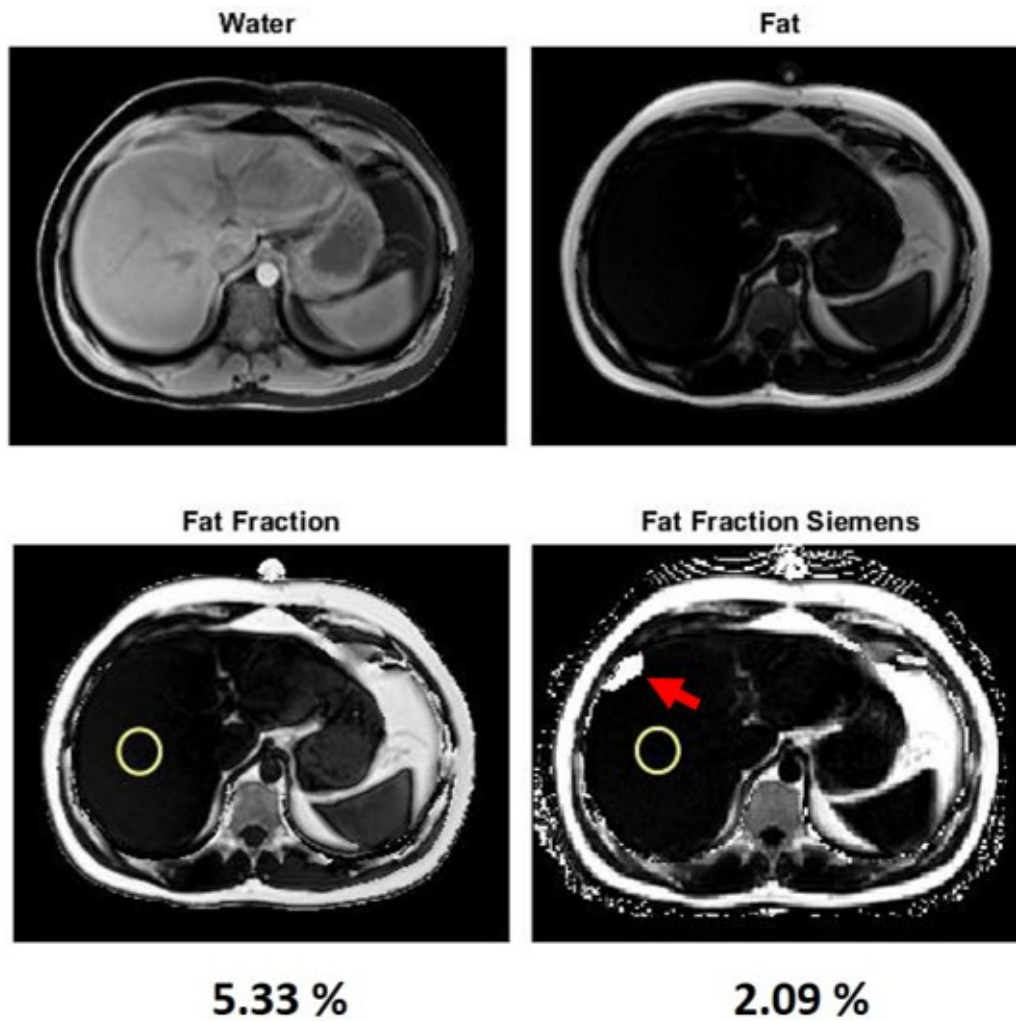


Figure 4.4: University of Mississippi - Liver Fat Fraction 3T

This data-set showed an artifact in the Siemens fat water separated images (not shown) and thus the artifact translated into the Siemens fat fraction image (shown here). The artifact is essentially a fat water swap. Notice, however, that when the data is processed using Hernando's graph-cut algorithm, the fat water separation does not result in any such artifact. Numerically though, there is a significant difference of fat-fraction values in the region of interest.

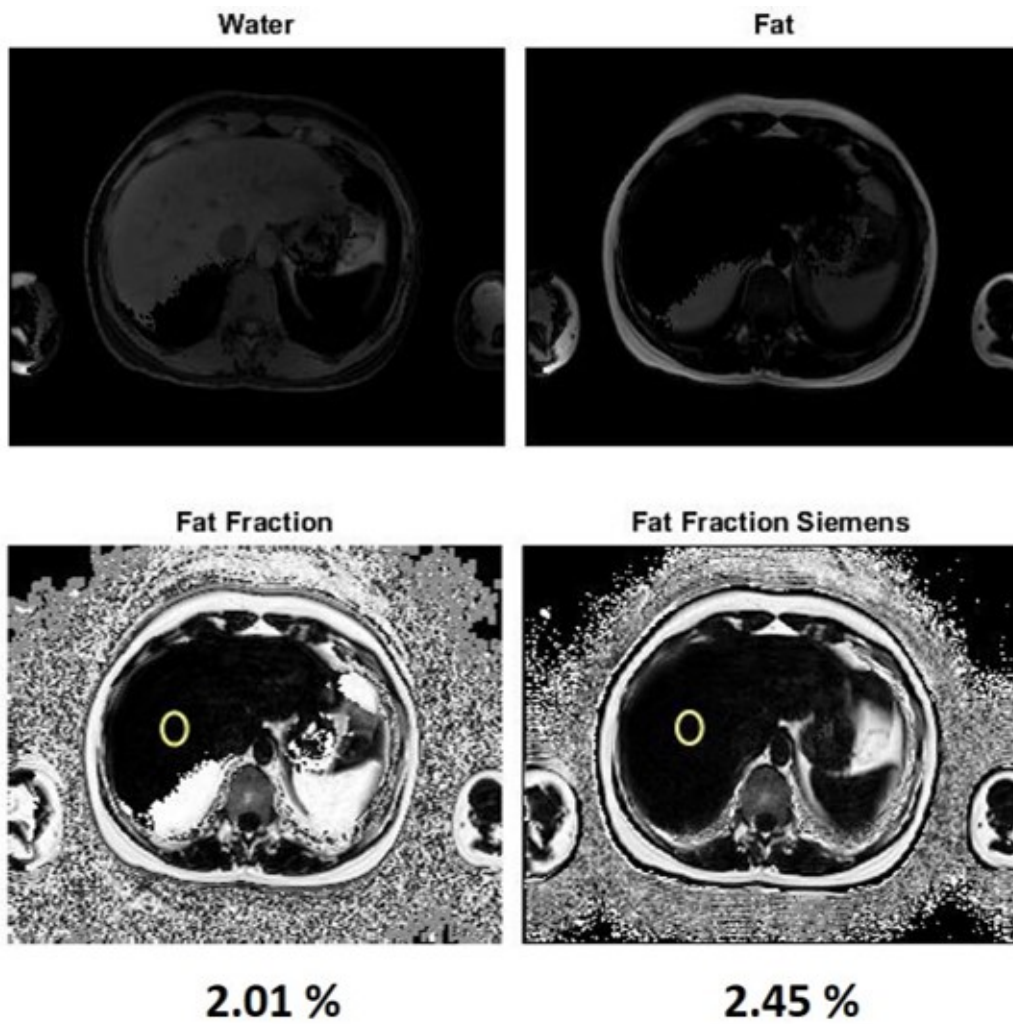


Figure 4.5: University of Alabama at Birmingham - Liver Fat Fraction 3T

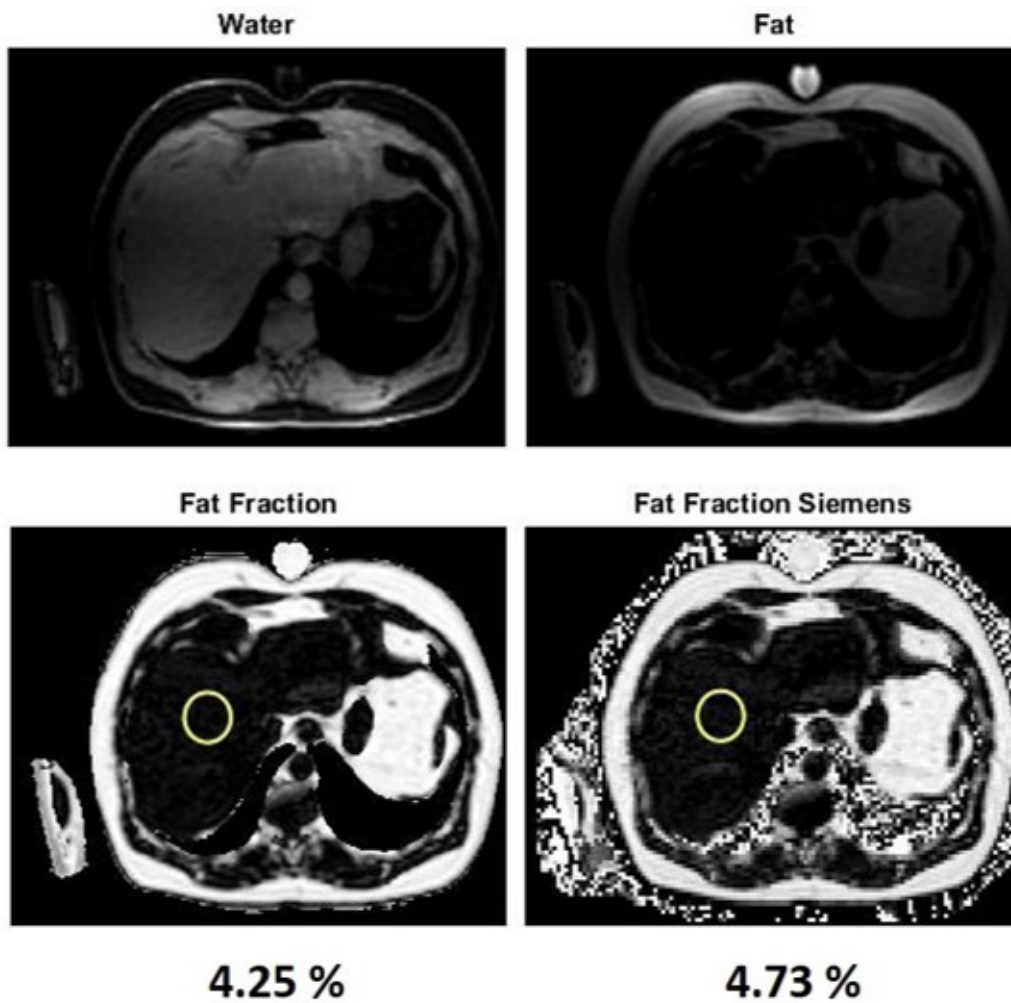


Figure 4.6: Auburn University - Liver Fat Fraction data-set #1 3T



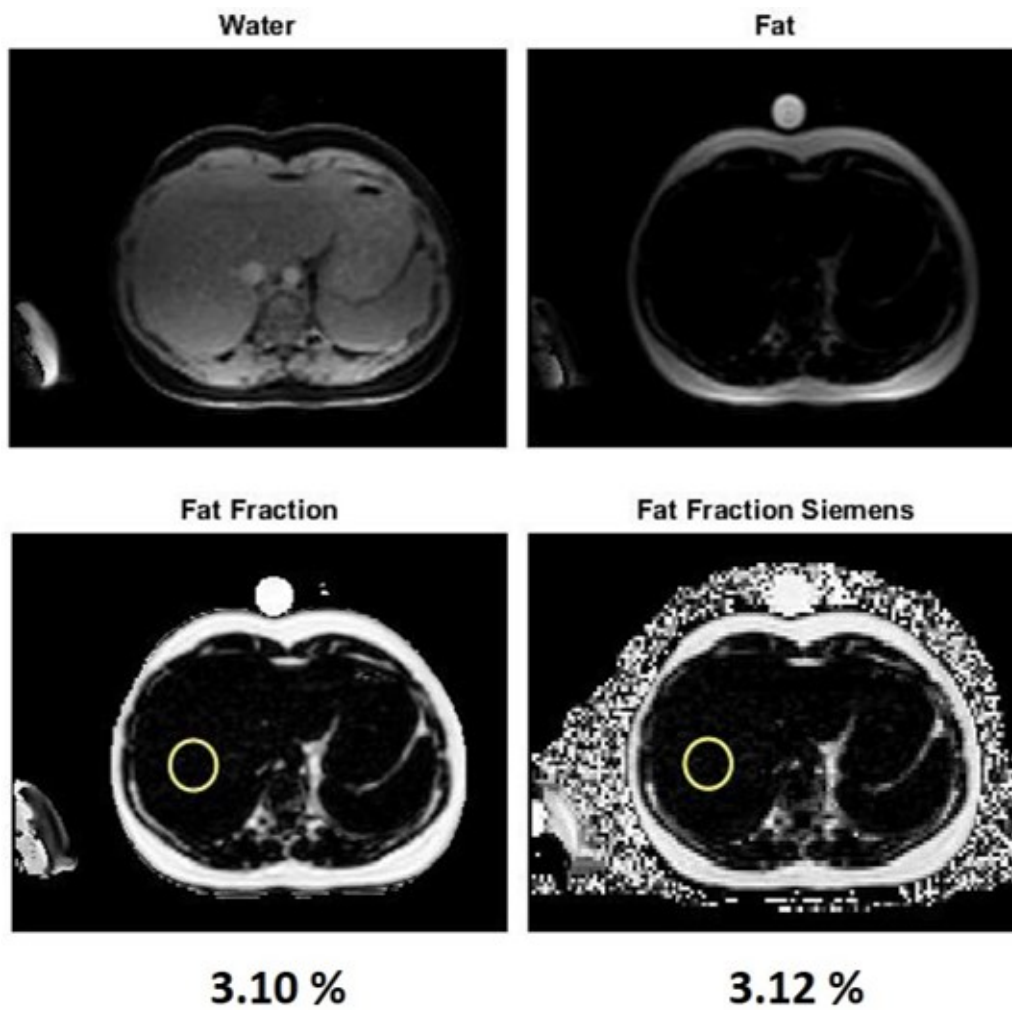


Figure 4.7: Auburn University - Liver Fat Fraction data-set #2 3T

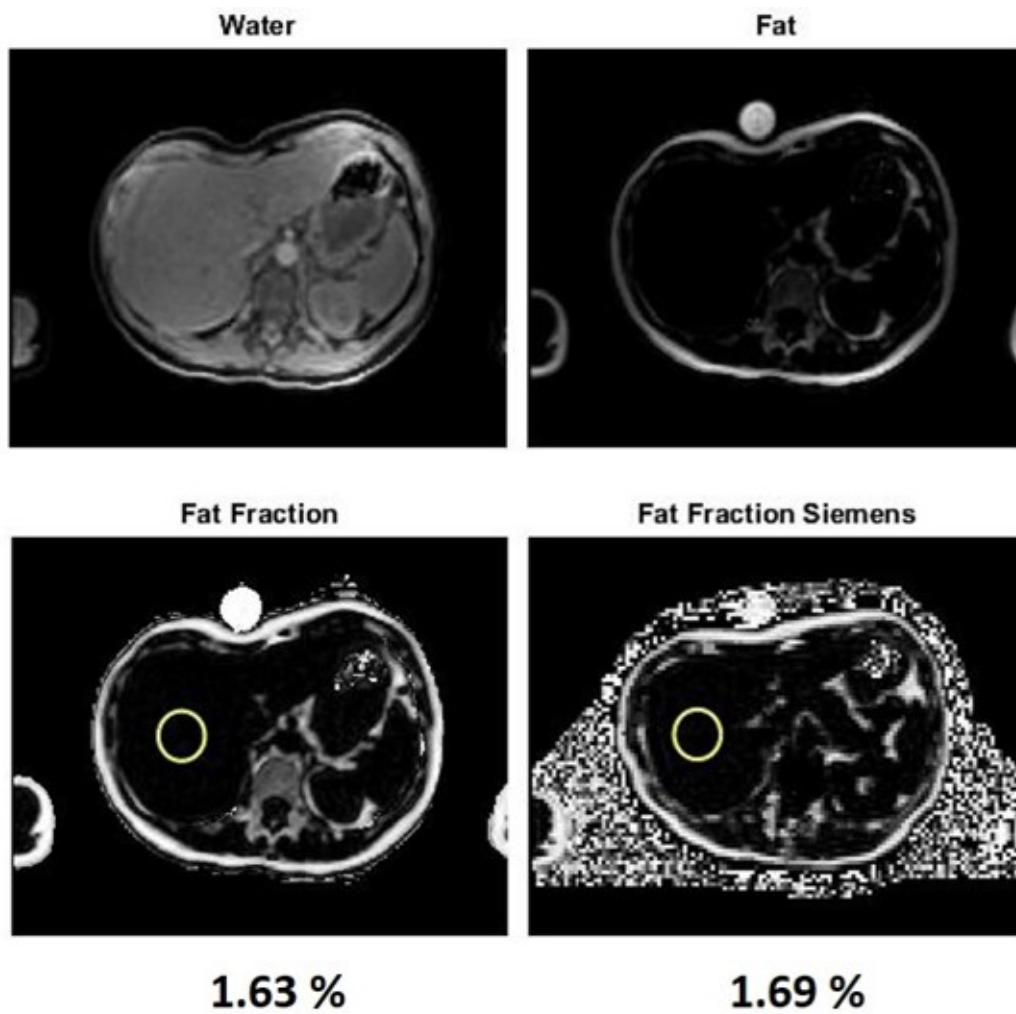


Figure 4.8: Auburn University - Liver Fat Fraction data-set #3 3T

## Chapter 5

### Conclusions and future recommendations

The phantom and the in-vivo study when put together present an accurate and reproducible approach to quantify intra-hepatocellular lipid.

A rigorous, dual-site (AU and UAB), dual-modal (MRS and MRI) and dual-strength (3T and 7T) validation of in-house constructed peanut oil phantoms followed optimizations in a standard spectroscopy sequence for a robust in-vivo protocol that also integrated a T2 correction scheme in liver fat quantification.

The imaging side of the study employed existing post-processing fat-water separation schemes on peanut-oil phantoms and saw an agreement with the spectroscopy data. This followed the quantification on multi-site in-vivo data, therefore, establishing a concrete setup for liver fat fraction quantification.

In terms of coverage of the liver, the imaging modality presents a larger coverage area compared to only a small voxel placed in the liver. However, as demonstrated, the accuracy of spectroscopic modality outweighs the imaging scheme. The limitation of a small coverage area in spectroscopy can and rather should be removed by using multiple voxels and averaging out the T2-corrected measurements.

One of the areas of future works in the algorithm development side could be to explore the effects of the adjacent slices on field inhomogeneity as existing algorithms only account for a 2D estimation of the field map. Another direction forwards is the classification of lipids in terms of monosaturated, disaturated or polyunsaturated lipid. Furthermore, there is a room to investigate the effects of iron overload in the liver which significantly shorten T2\* values and

therefore, affect the fat fraction in the liver and finally, these studies could be investigated on 7T which is more susceptible to field inhomogeneities and thus, a challenge in itself.

## References

- [1] Mantovani Alessandro, Byrne Christopher D., Bonora Enzo, and Targher Giovanni. Non-alcoholic fatty liver disease and risk of incident type 2 diabetes: a meta-analysis. *Diabetes Care*, 2018.
- [2] Paul Angulo. Nonalcoholic fatty liver disease. *The New England Journal of Medicine*, 2002.
- [3] T. Benkert, L. Feng, D. K. Sodickson, H. Chandarana, and K. T. Block. Free-breathing volumetric fat/water separation by combining radial sampling, compressed sensing, and parallel imaging. *Magnetic Resonance in Medicine*, 78(2):565–576, 2017.
- [4] J. Berglund, L. Johansson, H. Ahlstrom, and J. Kullberg. Three-point dixon method enables whole-body water and fat imaging of obese subjects. *Magnetic Resonance in Medicine*, 2010.
- [5] Johan Berglund. *Separation of Water and Fat Signal in Magnetic Resonance Imaging : Advances in Methods Based on Chemical Shift*. PhD thesis, Uppsala University, Radiology, 2011.
- [6] Johan Berglund, Hkan Ahlstrm, Lars Johansson, and Joel Kullberg. Two-point dixon method with flexible echo times. *Magnetic Resonance in Medicine*, 65(4):994–1004, 2011.
- [7] C. P. Bernard, G. P. Liney, D. J. Manton, L. W. Turnbull, and C. M. Langton. Comparison of fat quantification methods:a phantom study at 3.0t. *Journal of Magnetic Resonance Imaging*, 2008.

- [8] E. C. Bush, A. Gifford, C. L. Coolbaugh, T. F. Towse, B. M. Damon, and E. B. Welch. Fat-water phantoms for magnetic resonance imaging validation: A flexible and scalable protocol. *Journal of Visualized Experiments*, 2018.
- [9] Mark Bydder, Takeshi Yokoo, Huanzhou Yu, Michael Carl, Scott B. Reeder, and Claude B. Sirlin. Constraining the initial phase in water-fat separation. *Magnetic resonance imaging*, 29:216–221, February 2011.
- [10] Chen Cui. *MRI fat-water separation using graph search based methods*. PhD thesis, University of Iowa, 2017.
- [11] M. Doneva, P. Bornert, H. Eggers, A. Mertins, J. Pauly, and M. Lustig. Compressed sensing for chemical shift-based waterfat separation. *Magnetic Resonance in Medicine*, 2010.
- [12] H. Eggers, B. Brendel, A. Duijndam, and G. Herigault. Dual echo dixon imaging with flexible choice of echo times. *Magnetic Resonance in Medicine*, 2011.
- [13] Glover G. H. Multipoint dixon technique for water and fat proton and susceptibility imaging. *Journal of Magnetic Resonance Imaging*, 1(5):521–530, 1991.
- [14] V. P. Grover, J. M. Tognarelli, M. M. Crossey, I. J. Cox, S. D. Taylor-Robinson, and M. J. McPhail. Magnetic resonance imaging: Principles and techniques - lessons for clinicians. *Journal of clinical and experimental hepatology*, 2015.
- [15] W. N. Jr Hannah and S. A. Harrison. Nonalcoholic fatty liver disease and elastography: Incremental advances but work still to be done. *Hepatology*, 2016.
- [16] W. R. Hendee and C. J. Morgan. Magnetic resonance imaging: Part i - physical principles. *The Western journal of medicine*, 1984.
- [17] D. Hernando, C. D. G. Hines, H. Yu, and S. B. Reeder. Addressing phase errors in fat-water imaging using a mixed magnitude/complex fitting method. *Magnetic Resonance in Medicine*, 67(3):638–644, 2012.

- [18] D. Hernando, Haldar J. P., Sutton B. P., J. Ma, P. Kellman, and Liang Z. P. Joint estimation of water/fat images and field inhomogeneity map. *Magnetic Resonance in Medicine*, 2008.
- [19] D. Hernando, P. Kellman, J. P. Haldar, and Z.-P. Liang. Robust water/fat separation in the presence of large field inhomogeneities using a graph cut algorithm. *Magnetic Resonance in Medicine*, 63(1):79–90, 2010.
- [20] C. D. G. Hines, H. Yu, A. Shimakawa, C. A. McKenzie, J. H. Brittain, and S. B. Reeder. T1 independent,  $t_2^*$  corrected mri with accurate spectral modeling for quantification of fat: Validation in a fat-water-sprio phantom. *Journal of Magnetic Resonance Imaging*, 2009.
- [21] W. Huh, J. A. Fessler, and A. A. Samsonov. Water-fat decomposition with regularized field map. In *Magnetic Resonance in Medicine*, 2008.
- [22] Runge J. H., Nederveen A. J., J. Verheij, Beuers U. H., and J. Stoker. Comparison of mdixon and proton density liver fat fraction maps in patients suspected of nafld/nash with 1h-mrs as reference. *European Society of radiology*, 2015.
- [23] Ma Jingfei, Son Jong Bum, and Hazle John D. An improved region growing algorithm for phase correction in mri. *Magnetic Resonance in Medicine*, 2016.
- [24] K. Li, X. Wu, D. Z. Chen, and M. Sonka. Optimal surface segmentation in volumetric images, a graph-theoretic approach. *IEEE transactions on Pattern Analysis*, 2006.
- [25] C. Liu, C. A. McKenzie, H. Yu, J. H. Brittain, and S. B. Reeder. Fat quantification with ideal gradient echo imaging: Correction of bias from  $t_1$  and noise. *Magnetic Resonance in Medicine*, 58(2):354–364, 2007.
- [26] J. Ma. Dixon techniques for water and fat imaging. *Journal of Magnetic Resonance Imaging*, 28(3):543–558, 2008.
- [27] R. Patil and G. K. Sood. Non-alcoholic fatty liver disease and cardiovascular risk. *World journal of gastrointestinal pathophysiology*, 2017.

- [28] Pernilla Peterson. *Quantification of Fat Content and Fatty Acid Composition Using Magnetic Resonance Imaging*. PhD thesis, Medical Radiation Physics, Lund University, 2013.
- [29] S. B. Reeder, Zhifei Wen, Huanzhou Yu, Angel R. Pineda, Garry E. Gold, Michael Markl, and Norbert J. Pelc. Multicoil dixon chemical species separation with an iterative least-squares estimation method. *Magnetic Resonance in Medicine*, 51(1):35–45, 2004.
- [30] Reeder S. B., Cruite Irene, Hamilton Gavin, and Sirlin Claude B. Quantitative assessment of liver fat with magnetic resonance imaging and spectroscopy. *Journal of Magnetic Resonance Imaging*, 2011.
- [31] Sharma S. D., Hu H. H., and Nayak K. S. Accelerated t2\*-compensated fat fraction quantification using a joint parallel imaging and compressed sensing framework. *Journal of Magnetic Resonance Imaging*, 2013.
- [32] S. Saab, V. Manne, Nieto Jose, Schwimmer J. B., and Chalasani N. P. Nonalcoholic fatty liver disease in latinos. *Clinical Gastroenterology and Hepatology*, 2016.
- [33] Abraam S. Soliman. *Acquisition and Reconstruction Techniques for Fat Quantification Using Magnetic Resonance Imaging*. PhD thesis, The University of Western Ontario, 2014.
- [34] Fat Water Toolbox. Fat water separation: insights, applications and progress in mri. *ISMRM Scientific Workshop*: <https://www.ismrm.org/workshops/FatWater12/data.htm>, 2012.
- [35] Dixon W. T. Simple proton spectroscopic imaging. *Radiology*, 153(1):189–194, oct 1984.
- [36] Xiaoke Wang, Scott B. Reeder, and Diego Hernando. An acetone-based phantom for quantitative diffusion mri. *Journal of Magnetic Resonance Imaging*, 46(6):1683–1692, 2017.
- [37] Yi Wang, Debiao Li, E. Mark Haacke, and Jeffrey J. Brown. A three-point dixon method for water and fat separation using 2d and 3d gradient-echo techniques. *Journal of Magnetic Resonance Imaging*, 8(3):703–710, 1998.



- [38] Triplett William T., Baligand Celine, Forbes Sean C., Willcocks Rebecca J., Lott Donovan J., DeVos Soren, Pollaro Jim, Rooney William D., Sweeney H. Lee, Bonnemann Carsten G., Wang Dah-Jyuu, Vandenborne Krista, and Walter Glenn A. Chemical shift-based mri to measure fat fractions in dystrophic skeletal muscle. *Magnetic Resonance in Medicine*, 2014.
- [39] T. Yokoo, M. Shiehorteza, G. Hamilton, T. Wolfson, M. E. Schroeder, M. S. Middleton, M. Bydder, A. C. Gamst, Y. Kono, A. Kuo, H. M. Patton, S. Horgan, J. E. Lavine, J. B. Schwimmer, and C. B. Sirlin. Estimation of hepatic proton-density fat fraction by using MR imaging at 3.0 t. *Journal of Radiology*, 258(3):749–759, mar 2011.
- [40] H. Yu, S. B. Reeder, A. Shimakawa, J. H. Brittain, and N. J. Pelc. Field map estimation with a region growing scheme for iterative 3point waterfat decomposition. *Magnetic Resonance in Medicine*, 2005.
- [41] H. Yu, A. S. Shimakawa, S. B. Reeder, C. A. McKenzie, and J. H. Brittain. Magnitude fitting following phase sensitive water-fat separation to remove effects of phase errors. In *Magnetic Resonance in Medicine*, 2008.
- [42] Huanzhou Yu, Ann Shimakawa, Catherine D. G. Hines, Charles A. McKenzie, Gavin Hamilton, Claude B. Sirlin, Jean H. Brittain, and Scott B. Reeder. Combination of complex-based and magnitude-based multiecho water-fat separation for accurate quantification of fat-fraction. *Magnetic Resonance in Medicine*, 66(1):199–206, feb 2011.